The Concept of the Polarimetric Matched Signal & Image Filters:

Application to Radar Target versus Speckle Reduction & Optimal Background Clutter Discrimination in Microwave Sensing and Imaging

Wolfgang-Martin Boerner, Matthias Walther, and Andrew Constantin Segal
University of Illinois at Chicago
Department of Electrical Engineering and Computer Science
The Communications and Sensing Laboratory
UIC-EECS/CSL, 840 W. Taylor, SEL-4210, M/C 154
CHICAGO, ILLINOIS/USA 60680-4348, T/F: +[1](312) 996-5480/2456

ABSTRACT

When determining the nature of speckle in microwave POL-SAR image analysis, various known methods of speckle reduction are reviewed and compared for the purpose of enhancing image quality in polarimetric matched image filtering. Basic principles of the Polarimetric Matched Image Filter (PMIF) are presented and by utilizing the now widely used NASA-JPL C-Band POL-SAR data sets, collected over the San Francisco Bay area, the PMIF concept, together with various speckle reduction methods are verified and interpreted. Specific emphasis is placed on demonstrating the efficiency and usefulness of applying the PMIF method to the optimization of image discriminants in POL-SAR image analysis.

1. INTRODUCTION

In POL-SAR image analysis [22, 24, 31, 32, 34, 35, 57, 62, 66, 71, 72, 101, 113-117, 127, 128], one deals with remotely sensed images obtained through fully coherent recordings of the electromagnetic vector-wave interrogation with the reflecting surface which requires a subsequent complete interpretation of amplitude, phase and **polarization** information in the formulation of the contrast optimization algorithms.

POL-SAR image formation was developed - step-by-step - as an extension of amplitude-only SAR [57,77,79,99] and amplitude-only plus limited-phase SAR using one single, more often inappropriately chosen fixed transceiver antenna polarization state. Thus, as a result, only one single coefficient of the radar cross-section matrix [σ (AB)] for a specific fixed combination of transmit-versus-receive polarization states is measured for every resolution cell of the raw image measurements, i.e., on a pixel-by-pixel basis. As a result of this highly limited and incomplete recording of the electromagnetic vector wave nature, very essential "vector wave information", imprinted in the "polarization state transformation properties" of the scattered-versus-incident wave, is lost and a complete description or recovery of the scattering process is therefore not possible. The only way in which we can ensure that complete information on the scattering process is retained, in order to enable adaptive filtering in an image post-processing mode, is to devise a completely coherent (snapshot) vector wave measurement approach, i.e., in addition to complete amplitude and phase information, also completely coherent polarization information must be recovered on a pixel-by-pixel basis. For moving target scenarios, such measurements ought to be executed at extremely short time intervals well under the decorrelation periods of moving and vibrating scattering ensembles. For fixed, stationary scatterers, this was first accomplished in dual polarization microwave holography (Boerner, Gniss, Magura, 1974-1978 [11]), where it was demonstrated that the incoherent superposition of the four scattering cross-section components ($\sigma'_{AB} \approx |\, S'_{AB}\,|^2$) of the dual-polarization transmit/receive channel provide the complete "polarization basis (A,B) invariant image" on a pixel-by-pixel basis, i.e., the "span image":

$$\text{Span}\{\,[\,S\,]\,\} = |\,S'_{AA}\,|^2 + |\,S'_{AB}\,|^2 + |\,S'_{BA}\,|^2 + |\,S'_{BB}\,|^2\,,$$

as was shown and demonstrated clearly in [10,11,12]. In an extension of the polarimetric microwave holographic principle which does not allow for the complete recovery of the relative phase scattering matrix on a pixel-by-pixel basis, especially for moving target scenarios, step-by-step first quasi-polarimetric amplitude-only ($|HH|$ and $|HV|$, $|HH|$ and $|VV|$, or $|VH|$ and $|VV|$), then com-

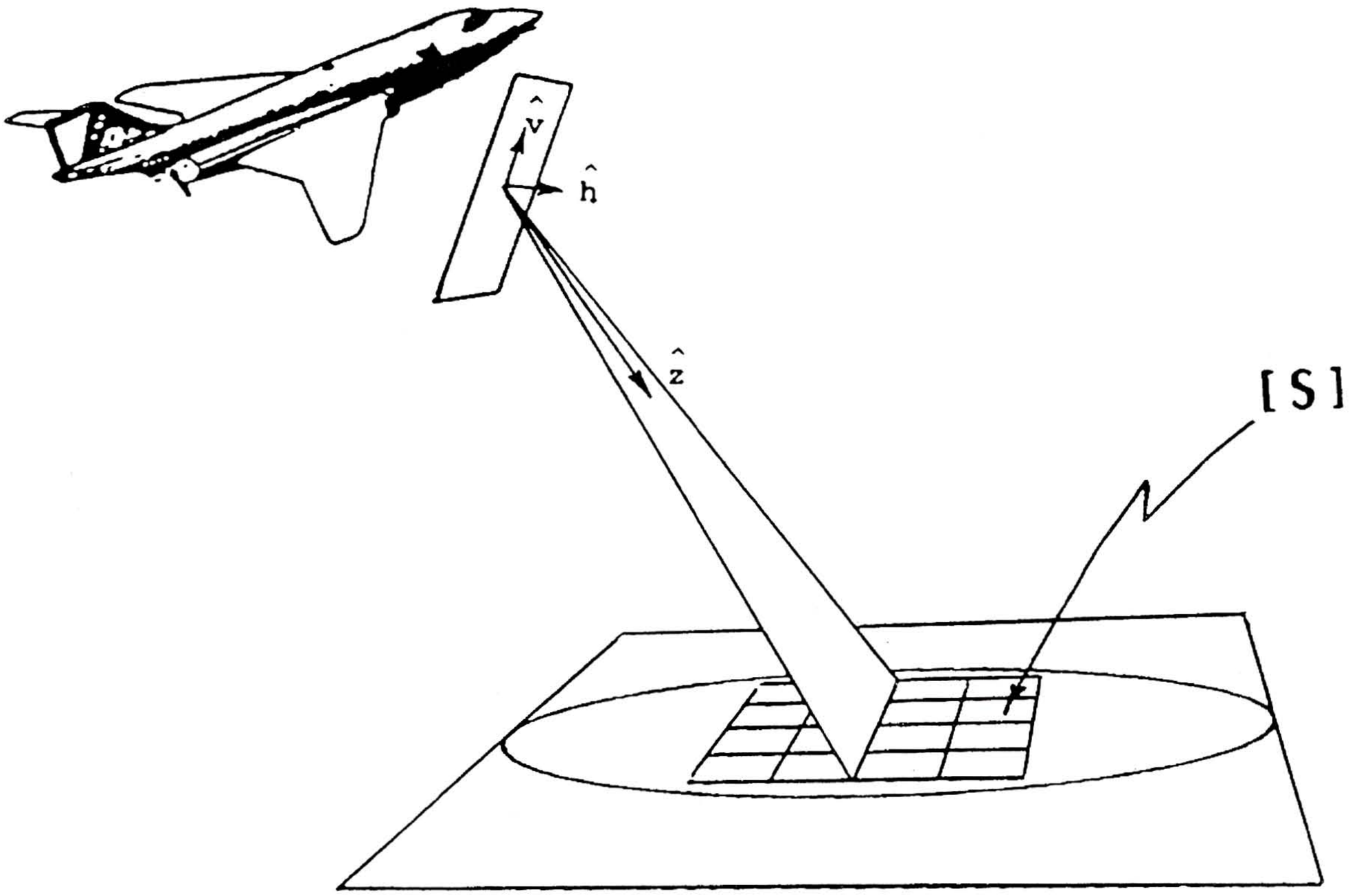

Fig. 1 - Schematic SAR System Configuration (Airplane with Ground Swath).

plete amplitude-only ($|HH|, |HV|, |VH|, |VV|$) polarimetric SAR systems were developed at the NASA Jet Propulsion Laboratory (JPL), leading to the development of the first complete relative phase POL-SAR polarimeter system. In these complete POL-SAR polarimeter systems, a sequence of orthogonally polarized waves is transmitted, and the received waves are decomposed into two orthogonally (co/cross)-polarized components which enter two identical, coherent receiver channels. Due to the advent of supra-fast orthogonal polarization state switching and real-time processing devices, completely coherent polarization diversity in the receiver is accomplished by coherent transmission polarization diversity, so that the complete, coherent 2x2 Sinclair radar scattering matrix [S] or the 4x4 Mueller radar reflection matrix (separately for the co/cross-polarized channels: $[M_{c/x}]$ can be recovered on a pixel-by-pixel basis [34,58,60-65]. Thus, with the advent of these very sophisticated coherent orthogonal dual-channel polarization/transceiver POL-SAR collecting devices, complete, electromagnetic vector wave image information has become available to us but the full potential of which has neither been fully comprehended nor exhausted.

Since complete scattering matrix information on a pixel-by-pixel basis can be made available also for the non-symmetric general bistatic and non-reciprocal cases, entire new image post-processing concepts will soon be developed and applied, which eventually will permit true optimum separation of desirable scatterer (target) from undesirable scatterer (clutter) information, and at the same time, novel, hitherto unthought of speckle reduction schemes, will be implemented in practical applications. The fully coherent recording of the electromagnetic vector wave image information also allows for a sequential step-by-step elimination of sources of noise and speckle accumulated during the entire image acquisition and storage process, by applying proper calibration and intermediate, coherent control signal information. Provided, that the effective footprint per illuminated scattering scene as well as the acquisition time per pixel scattering matrix can be reduced significantly, new methods of reducing incoherent, temporal, and spatial speckle can be derived, and also improved internal processor noise reduction should be feasible. Thus, by further advancing the concepts of POL-SAR imaging to include motional polarimetric doppler information on an pixel-by-pixel basis as well, relative

target motion can be frozen, therefore providing the means of obtaining almost ideally "clean" images. Instead of further pursuing the development of such advanced concepts, in the following sections emphasis is placed on introducing polarimetric speckle and clutter reduction with simultaneous optimization of image contrast procedures on the basis of the currently available data sets.
In order to improve on the image feature-versus-background clutter-plus-speckle contrast, we are introducing here the concept of the Polarimetric Matched Image Filter (PMIF) with the specific goal of optimizing the image discriminants in POL-SAR image analysis. Therefore, after introducing the concept of the Polarimetric Matched Image Filter (PMIF), we will then demonstrate how image discriminants can be optimized both against background clutter and speckle.

1.1 What is Speckle - Coherent vs. Partially Polarized Case

Speckle is seen as a random intensity (amplitude, phase) distribution which is caused by the reflection of some incident, coherent electromagnetic vector wave (amplitude, phase and **polarization**) from a rough surface. A surface is considered rough if the heights between its peaks and valleys differ by at least one wavelength of the incident radiation (Goodman [45,46], Dainty [28,29]). In the optical (laser) or microwave (POL-SAR) region, all natural land and water surfaces tend to be rough, therefore causing an abundance of (a) depolarization and (b) speckle in coherent reflected images.
(a) **Depolarization effects** along a rough surface at microwave frequencies can be attributed to specific geometries such as linear stalks of plants and trees, roads and buildings, coastlines and various geologic and marine features [7,10,23,25,27,34-37,42-44,53,69,73,92,105-110,128-129] i.e., whenever the index of refraction (dielectric permittivity) and/or conductivity change abruptly; and so also the electric surface curvature [39,83,94,100]. These geometries can be simulated mathematically as dipoles, corner reflectors, di/tri/tetrahedrals, etc. [115]. Some prominent post-imaging methods will be mentioned which are capable of enhancing POL-SAR images. When using coherent POL-SAR measurement data sets, the 'operator' relating the transmitted and reflected fields is known as the complete complex-valued 2x2 (Sinclair) scattering matrix [S] (or its related form of the 4x4 Mueller matrix [M] for the partially coherent or also partially polarized cases). Whereas in the partially coherent case no assumptions about the coherent nature of the incident field can be made, in the partially polarized case we assume the degree of polarization together with the state of polarization of the incident wave to be known. Thus, the incoherent spatial and temporal nature of the scattering surface properties contributes to the random depolarization phenomenon, which in turn is exhibited in the scattered waves and identified in the form of the Stokes reflection matrix. The 2x2 Sinclair matrix, [S], may, however, be thought to be a complete characterization of the scatterer at that image point at one particular frequency, aspect, and for a single 'point scatterer', under the assumption of a snapshot image.

Remark: This approximation may be acceptable, due to the fact that the individual pixel matrices $[S]_i$ are collected far below the decorrelation time of clutter but not necessarily below the scintillation periods of speckle which requires further experimental analysis and testing. Furthermore, the effective footprint of the interrogating central beam may be considered sufficiently small for crudely applying a "quasi-point scatterer" approximation which also requires further extensive analysis.

These coherent pixel scattering matrices consist of complex-valued co-polarization (Co-Pol) and cross-polarization (X-Pol) elements, expressing the amplitude and phase by which the scattered surface resolution cell transforms the incident polarization and depolarizes, i.e., alters the polarization state and the degree of polarization of an incident plane wave, respectively. Assuming that the degree of polarization remains unchanged, the scattering matrix [S] is an excellent starting point for image analysis [11-22, 63-67, 113-117, 128-129], allowing for mathematical manipulations of amplitude and phase in the complex domain. In fact, without implementing the [S] matrix approach, optimal image pixel post-processing would remain rather primitive and restricted.
(b) **Speckle** can also be seen as a depolarization phenomenon; it, however, does not seem to be directly related to a particular surface geometry or to specific roughness patterns at the region where speckle appears on the image [29]. Even when using highly coherent, monochromatic incident radiation, the image acquires a peculiar granularity which does not exhibit any detailed structure or signature of any specific sort. Because of its random nature and the great amount of data in the image, speckle is best described and treated by first- and second-order statistics. J.W. Goodman coined the phrase of "**a Random Walk of Phasors in the Complex Plane**", i.e., "the amplitude of the electric field at a given observation point consists of a multitude of de-phased contributions from different scattering regions of the rough surface" [28-29,45-46]. Making the assumption that all elementary complex vectors, i.e., the amplitude and phase of each image cell (pixel), are statistically independent of each other, the phases are uniformly distributed which implies that the

surface is rough by many times the 2 π radians of the incident wavelength. It can be shown that average values of separate ensembles of the real and imaginary parts of the resultant field have zero means, identical variances, and that they are uncorrelated [45]. The next step is to show that, given the large number of elementary phasor contributions, and by applying the Central Limit Theorem [46, 78, 112] that the real and imaginary parts of the reflected fields are asymptotically approaching a Gaussian distribution. It turns out that the joint probability density function (PDF) of the real and imaginary parts of the field is indeed of the circular Gaussian kind for most cases [45]. Hence, speckle seems to be "well-behaved" in a statistical sense. Whereas above considerations apply to "spatially distributed random walk of phasors", similar considerations can be deduced for temporal scintillations.

Weak Scattering

A useful statistical approach to scattering with non-Gaussian properties is known as K-distribution. In radar science, the K-distribution is used as a model for scattering with a non-uniform distribution of phase due to fluctuations in the target (e.g. motional/orientation, turbulence, etc.) The non-uniformity of phase implies that phase is biased or correlated. The scattered electric field vector is essentially a two-dimensional vector which "may be represented as the resultant of a random walk in a plane with a negative binomial distribution of the number of steps [6]. This distribution takes on the von Mises form

$$P(\phi) = \frac{\exp(\upsilon \cos\phi)}{2\pi I_0(\upsilon)} \tag{1a}$$

where I_0 is the modified Bessel function of the first kind and υ is a parameter representing the limits for the distribution,

$$P(\phi) = 1/2\pi\,;\ \upsilon \to 0\,,$$
$$P(\phi) = \delta(\phi)\,;\ \upsilon \to \infty \tag{1b}$$

Meanwhile, this limited von Mises form of the K-distribution has been generalized to a random walk in any number of dimensions [6,55,56,93].

We are only going this far in our introduction to the very important subject of non-Gaussian scattering which holds great promises for the explanation and mathematical treatment of numerous scattering phenomena with non-Gaussian characteristics also in POL-SAR image analysis. In summary, regarding speckle in POL-SAR imagery, we need to investigate which of the recently developed methods of speckle reduction produces reliable results and can be further developed towards automatic speckle reduction algorithms and can be used during future remote sensing missions for the detection of low RCS targets in severe dynamic background clutter. In Section 2 of this paper, speckle and noise reduction schemes are presented from a historic perspective and specific short-comings of previous non-polarimetric approaches are pointed out as we go along. Whereas the real and imaginary part statistics of the individual scattering matrix elements may be "well-behaved", it can be shown that the same does not hold true in general for the four (sixteen) scattering matrix elements of the Sinclair (Mueller) matrix. For example, it is well known that for sea-surface backscatter, the HH component statistics differs significantly from that of the HV, VH, and VV statistics [70, 82, 96].

1.2 Basic Concepts of the Polarimetric Matched Image Filter

The large amount of randomly distributed and mutually independent data of an image requires that an efficient mathematical method be used to generate an estimate of the range of the values. The probability density function, for instance, takes a data set and determines the distribution of intensities, for example, which may look like a bell-shaped curve when plotted. The advantage of grouping data statistically lies in the fact that image data of ocean, land, vegetation, etc. can be differentiated by their characteristic probability density functions (PDFs) which is a useful tool in the classification of terrain types in an image. Furthermore, this approach in POL-SAR image analysis is further amplified by the observation of the different scattering matrix elements S_{AB} posing different PDFs among each other as well as for different elliptic polarization bases (AB), e.g., linear, right/left circular or general elliptical.

1.3 Approaches for Optimization of Image Discriminants in POL-SAR Image Analysis

It can be shown that the log gradient dielectric and conductivity components

$$\vec{A} \bullet (\nabla \varepsilon/\varepsilon) \text{ and } \vec{E} \bullet (\nabla \sigma/\sigma) \tag{2}$$

of the inhomogeneous vector wave equation are highly polarization sensitive (Stratton [100]), resulting in strong polarization transformations of the incident wave which show up in the polarimetric image evaluation. These "polarization state transformation" terms of the inhomogeneous vector wave equation, identify not only sudden major transformation changes at discontinuities but also imply gradual polarization state transformations as a wave propagates through such an inhomogeneous medium for which these terms are non-negligible [22, pp. 1105-1117, 124]

2. METHODS OF SPECKLE REDUCTION

Speckle can be dealt with in several ways. One way of reducing or eliminating speckle is by filtering or masking the image by means of digitized intensity attenuation or statistical averaging of parts or of the entire image (Section 2.1)[8,47,49-51,54,87,90,97,125]. Another method is to apply principles of probability and communications if speckle is considered noise (Section 2.2), in the sense that it distorts the actual image information [3,80]. A third method (Section 3) treats speckle as a seemingly random contribution of residual phasors by all parts of the image. Speckle may be reduced by finding the maximum power of the reflected fields in an attempt to optimize the image for high contrast between terrain types [63-67]. In any case *a priori* electromagnetic means of speckle removal must be applied before any other image restoration is applied.
Specifically, Section 2.1 consists of a brief overview of "traditional" image enhancement methods, based on computer-numeric digital image manipulation, which are still used to improve satellite, medical or industrial images cosmetically. After determining the range of pixel intensities of the image, specific subranges are selected and either smoothed or sharpened in order to show some desired visual information. These methods work very well when showing images of large areas encompassing such events as oil slicks, weather/ocean current patterns, geologic formations, agricultural/pollution maps, arctic ice range and medical imaging, etc.
In Section 2.2, an intermittent statistical approach of speckle reduction, based on polarimetric scattering matrix manipulations is summarized which takes advantage of complex-valued, coherent polarization data. This approach is intermittent on our way to image manipulation and classification, based of electromagnetic principles, in that the span of an image is used as an entry point into the subject, but then it is treated merely from a statistical viewpoint, borrowed from electronic communications theory.
It is the intent of this paper to stress these aspects in an introductory manner in order to encourage the expert reader to further advance on these approaches. Although these methods have merit, it will be shown in Section 3, that the polarimetric matched image filter (PMIF) approach is more promising from an electromagnetic point of view and lends itself to some very sophisticated methods of image manipulation and correction of errors through computer-based simulation of the physical radar system.

2.1 Speckle Reduction through Computer-Numeric Filtering

When image data are manipulated to emphasize specific details, it frequently happens that the image loses some quality, i.e., important visible image features degrade. Sometimes, extraneous information in the form of noise may be introduced during any conversion process.
Since the inception of radar (and later on of lidar), many basic enhancement and more sophisticated image restoration techniques have been developed to compensate for image degradation and to enhance specific image features. The majority of enhancement methods were developed for optical and infrared imaging systems (lidar). They consist of gray scale adjustments of digitized images (i.e., assigning attenuation values to intensities and piece-wise linear quantization for contrast enhancement), deblurring (i.e., deconvolution in the spectral domain) and smoothing (i.e., averaging and weighting of pixels). On a more sophisticated level, image restoration is concerned with the emphasis of select feature extraction and the simultaneous suppression of undesirable information in the image with the goal of correcting for a specific degradation process. Most of the time, the degradation operator is unknown or difficult to define because it may be non-linear, hence image restoration consists primarily of a trial-and-error approach. The best restoration method is one which is tunable, i.e., in which the enhancement parameters can be varied continuously as the image is being enhanced and visually evaluated simultaneously [116]. The following section consists of an overview and introduction to the elementary methods of image enhancement, followed by an evaluation of their advantages and short-comings and some suggestions as to which ones of these fundamental methods are most suitable for speckle reduction.

2.1.1 Gray Scale Modifications and Transformations

One of the most useful methods is gray scale modification which has two forms, i.e., gray level correction of individual pixels or image regions and gray scale transformation which changes the distribution of the gray level for the entire image [2]. Gray scale transformations involve histogramming of the original data, whereby spurious data points are neglected. Hence, pixel brightness is redistributed over a range of brightness values, thus making desirable (operator-controlled) gray level adjustments. As for gray level correction, if an image was mapped non-uniformly (e.g., due to vignetting of the receiving system), the picture can be calibrated on a picture of uniform field of known brightness provided that [90]:

$$g(x, y) = e(x, y) f(x, y) \tag{3}$$

where f(x,y) corresponds to the ideal gray level of a picture point (x,y), and g(x,y) is the actual gray level at that point and the function e(x,y) is a calibration function.

2.1.2 Gray Scale Transformations

Gray scale transformation over the entire image or a sizable region of the image increases image contrast [48,51,90]. For instance, to increase contrast of an image which has fewer gray levels than the imaging computer is capable of handling, i.e., the image is "underexposed", the gray scale can be stretched to encompass the entire allowable range. Similarly, if it turns out that most of the picture elements occupy just a subrange, which means that the image is compressed, a piece-wise linear transformation stretch of the gray scale interval may be applicable. Therefore, it is possible to stretch selected regions of the gray scale to enhance image details at the cost of compressing other less desirable regions. This is one method by which speckle can be reduced, if speckle occurs within a limited range of intensities.

This contrasting technique of mapping different gray levels of the picture can also be applied to false coloration of the image, where different hues are assigned to certain brightness values or ranges. Colors can greatly enhance the visibility of details in the image.

2.1.3 Sharpening

Averaging over a number of pixels, which corresponds to an integration operation on the image, tends to blur the image. Averaging also has a destabilizing effect on higher frequencies. Differentiation, however, can be used to deblur or sharpen the image. Furthermore, high spatial frequencies should be emphasized in the process of picture sharpening. If possible, the image should be rid of noise or speckle patterns before applying any sharpening methods, because at high frequencies the noise signals may overpower the image signals. Any attempt of differentiating should be done by means of an isotropic linear derivative operator involving derivatives of even orders [87]. Isotropy or rotation invariance is desirable, because it should be possible to sharpen blurred edges and lines going in any direction of the image.

2.1.4 The Laplacian Operator

The following linear derivative operator

$$\nabla^2 f = \frac{\partial^2 f}{\partial x^2} + \frac{\partial^2 f}{\partial y^2} \tag{4a}$$

is also known as a two-dimensional Laplacian. Suppose a blurred picture results from a diffusion process (e.g. averaging), satisfying the following partial differential equation:

$$\frac{\partial g}{\partial t} = k \nabla^2 g \tag{4b}$$

where g is a function of x,y and t, k is const., and g(x,y,0) represents the unblurred picture f(x,y). At sequence $t=\tau > 0$, $g(x,y,\tau)$ can be expanded into a Taylor series centered on $t=\tau$, resulting in the following first order term expression

$$f = g - k\tau \nabla^2 g \tag{4c}$$

Higher order terms are generally ignored in order to reduce the time it takes to process large image arrays. Digital images may be processed by following the digital analog to a Laplacian

$$\begin{aligned}\nabla^2 f(i,j) &= \nabla_x^2 f(i,j) + \nabla_y^2 f(i,j) \\ &= [f(i+1,j) + f(i-1,j) + f(i,j+1) \\ &\quad + f(i,j-1)] - 4f(i,j)\end{aligned} \tag{5a}$$

which is the same as

$$f(i,j) - \frac{1}{4}[f(i+1,j) + f(i-1,j) + f(i,j+1) + f(i,j-1)] \tag{5b}$$

where each pixel is averaged together with its horizontal and vertical neighbors. Hence, the digital Laplacian of an image is a method of subtracting a blurred, i.e., averaged version of f itself. Other types of Laplacian-type operators can be used such as a 3x3 neighborhood Laplacian, consisting of eight horizontal, vertical and diagonal neighbors, or using weighted averages over the neighborhood.

2.1.5 High Emphasis Filtering

Mathematically, high-emphasis filtering corresponds to a subtraction of the Laplacian from every image point such that

$$\begin{aligned}&f(i,j) - \nabla^2 f(i,j) = \\ &f(i,j) + 4\left[f(i,j) - \frac{1}{4}\{f(i+1,j) + f(i-1,j) \right. \\ &\left. + f(i,j) + f(i,j+1) + f(i,j-1)\}\right]\end{aligned} \tag{6a}$$

As a result of this operation, the low frequencies in f are canceled out while the high frequencies remain intact [90]. Consequently, an addition of a multiple of the difference operator to f should boost the high frequencies, thus sharpen the image and enhance edges and lines. This filter which is passed over every picture element of the image,

analogous to a convolution operation, might look like

$$\begin{array}{ccc} & 1 & \\ 1 & -4 & 1 \\ & 1 & \end{array} \quad or \quad \begin{array}{ccc} & -1 & \\ -1 & 4 & -1 \\ & -1 & \end{array} \tag{6b}$$

where the first filter reduces the pixel intensity and the second filter enhances pixel intensity.

Sometimes, high-emphasis filtering is used in conjunction with logarithmic gray scale transformations. This method reduces shading effects which occur in satellite pictures of planetary bodies, yet it preserves edges and lines in the image. High-emphasis filtering is the most sophisticated method among computer-numeric approaches of practical image enhancement and is very common in satellite and medical imagery.

2.1.6 Smoothing Operators

Smoothing methods are often used to remove speckly noise. If not applied properly, however, smoothing has the tendency of blurring sharp edges and lines. To remove periodic noise, for instance, a Fourier transform can be taken of the image and filters can be used to remove the lines or regions corresponding to speckle in the Fourier space. The deblurred image is then obtained by taking the inverse Fourier transform. This can be done by zeroing out the frequency components related to noise or removing by interpolation or shifting those noisy frequency segments, leaving the remaining image intact. If noise is multiplicative, however, smoothing in this manner would not be very successful since the undesirable frequency components cannot be isolated so easily. Noise, occurring in isolated pixels (salt-and-pepper noise), which is more typical of speckle in SAR images, could be isolated by comparing each pixel with the intensity levels of its neighbors. A large difference in intensity between neighboring pixels might be an indication of random noise (speckle) which is removed by interpolation, i.e., averaging with its neighbors, as described in the previous section. The use of smoothing methods which are based on weighted averages, however, is not a well-defined scheme of enhancing the image and as long as the operator has to assign weights to the filter, such methods would not be suitable for automation. Here, we also emphasize that without the availability of the complete incoherent span information such methods remain dubious.

2.1.7 Point-Wise Averaging

Another class of smoothing methods is point-wise averaging which distinguish themselves from the previous one in that they do not depend on the identification and removal of noise [90]. Instead, a scheme is used to weaken the impact of noise on the image by averaging neighboring pixel values. Averaging, however, tends to blur the picture and degrades details of lines and edges. As for noise, however, averaging of pixel values decreases the amplitude of speckly noise fluctuations, thus a delicate compromise is reached when using this method. The method of averaging works best if several independent copies are made of the same blurred image for which noise can be reduced by point-wise averaging the same pixels in the copies, where

$$f(x, y) = \left(\frac{1}{n}\right) \sum_{i-1}^{n} f_i(x, y) \tag{7}$$

The method of point-wise averaging is also used for images which have symmetry or periodic noise structures.

One great disadvantage of the smoothing methods described so far is that averaging is done across lines and edges. To avoid this, an edge or line detector might be used first followed by a smoothing operator which skips the lines and edges. A more refined edge detector would be one which performs a directional averaging, i.e., averaging and enhancing lines and edges by themselves but ignoring nearby pixels.

Another useful averaging method is called median or rank filtering, whereby each pixel value is replaced by the median of the values of its neighborhood. This method eliminates spikes and flattens oscillations which are the most common occurrences of speckle in images.

2.1.8 Non-Linear Filtering

Other filtering approaches can be generalized into a class of non-linear filters. These filters are different from the previously discussed filters since they do not behave in a linear fashion:

$$f(image1 + image2) \neq f(image1) + f(image2) \tag{8}$$

where f is the filtering function. The most common non-linear filter is the median filter which replaces the center pixel value with the median of the neighborhood pixels around the center pixel [92]. This filter is non-linear and changes the statistics of the original image (mean and variance of the pixel values) but does not introduce any new pixel intensities in the filtered image, unlike linear filters. Median filters are reasonably effective on speckle noise since speckle tends to produce very large and very small pixel values which are eliminated using the median operation. Other non-linear filters include rank filters which are a generalization of medians using histograms of the neighboring pixels to determine a filtered pixel value and several non-linear image restoration techniques.

2.1.9 Section Summary: Need for a Different Approach

We have reviewed various standard computer-numerical image enhancement and speckle reduction methods which we consider pertinent to POL-SAR image contrast analysis. However, we have not attempted to exhaust all possible methods but rather wished to emphasize their incompleteness and that we need to look for other more complete electromagnetic vector wave approaches.

The most prominent short-coming of these image enhancement methods are that they require human intervention for two reasons: visual selection of areas to be enhanced by means of colors, gray-scale, etc. and human interpretation of the visual information, since no algorithms are applied to make any decisions on the image elements. In order to steer toward the implementation of more sound approaches, we need to take recourse to basic electromagnetic theory and we need to deliberate on how electromagnetic vector waves interact with distributed scattering centers, etc., and then form the scattered imaging wave components. In a next step, in a truly electromagnetic approach, we then need to investigate in depth the entire process of vector/tensor image formation.

Modern POL-SAR image analysis provides such a new approach and it consists of complex-valued, coherent polarization data, giving rise to amplitude and phase manipulations of the images. As a rule, POL-SAR data are provided in the form of 2x2 Sinclair or 4x4 Mueller scattering matrices which contain all the polarization-transforming signature parameters on a pixel-by-pixel basis, i.e., the effects due to a surface which in some manner reflects an incident electromagnetic plane wave. Hence, POL-SAR data which contain a wealth of additional useful information about scanned terrain, lend themselves to a more advanced physico-mathematical treatment of the scattering elements which open up entirely new avenues for computer-enhanced and automatic computer-based image recognition.

It is the intent of this paper to stress these aspects in an introductory manner in order to encourage the expert reader to further advance and expand on these approaches. However, before introducing the concepts of a truly polarimetric matched image filter approach, the intermittent statistical approach of speckle reduction based on polarimetric scattering matrix manipulations is summarized in the next Section [120].

2.2 Speckle Reduction through Statistical Averaging of the Scattering Matrix Elements

Having recovered the complete vector wave information on the image on a pixel-by-pixel basis instead of being given just one radar cross-section or the three radar cross-sections σ_{HH} , σ_{VV} , and $\sigma_{HV} = \sigma_{VH}$, we are now given four complex elements ($S_{\mu\upsilon}$, μ , $\upsilon = 1,2$) of the scattering matrix [S] to work with which has certainly increased the degree of freedom in terms of image manipulation and thus may or also may not assist in possible speckle reduction, if properly utilized. Thus, with the advent of complete polarimetric high-resolution coherent radar and SAR imaging systems, there now exists the possibility of optimally processing the coherent scattering matrix via individual and clustered pixel manipulation in such a way as to reduce the speckle content of specific SAR image regions.

In a paper by Boerner [13] it was demonstrated that span images are invariant to polarization basis transformation, and that the span images appear to the eye as having less speckle than usual single polarization SAR images which is consistent with the fact that the human eye processes images in a mostly incoherent manner. In this case, each pixel of a scan image is constructed from the incoherent superimposition of the four complex scattering matrix elements $\sigma_{AA} = |S'_{AA}|^2$, $\sigma_{AB} = |S'_{AB}|^2$, $\sigma_{BA} = |S'BA|^2$, and $\sigma_{BB} = |S'_{BB}|^2$ which reduce to three elements in the monostatic reciprocal case, where $S'_{AB} = S'_{BA'}$ so that

$$Span\{[S(AB = BA)]\} = |S'_{AA}|^2 + 2|S'_{AB}|^2 + |S'_{BB}|^2 \tag{9a}$$

furthermore, it is shown in [20,21] that

$$Det\{[S(AB = BA)]\} = S'_{AA}S'_{BB} - (S'_{AB})^2 = S_{HH}S_{VV} - (S_{HV})^2 \tag{9b}$$

and Kennaugh [59] introduced the 'effective radar cross-section (ECS)' also denoted as the 'polarimetric excess':

$$\sigma = (SPAN\{[S]\} + 2|Det\{[S]\}|) \tag{9c}$$

which are important invariants in radar polarimetry [12, 14-22] and especially in POL-SAR imaging [21].

Next, to this non-coherent superposition of the three polarimetric images for single elements ($|S_{HH}|^2$ image, $|S_{VV}|^2$ image, and $|S_{VH}|^2$ image), there may exist other methods of polarimetrically minimizing speckle by incorporating complete polarimetric information. In order to determine such possible methods, a covariance matrix method is introduced next, before proposing the complete, coherent polarimetric operator of Kennaugh [58,59] and Huynen's polarization concept [52] for implementation.

2.2.1 The Polarimetric Feature Vectors and the Polarimetric Covariance Matrix Formulation

Utilizing these invariants (9a-c), first introduced into polarimetric microwave imaging in [14-16], the concept of the polarimetric feature vector and the corresponding polarimetric covariance matrix [Σ] are introduced. At each instantaneous state of time any stochastic target is completely described by a corresponding scattering matrix [S'(AB)] or equivalently by a polarimetric feature vector $\vec{\Omega}$ (AB). For the general non-reciprocal and/or bistatic case that scattering matrix [S'(AB)] is non-symmetric, i.e., $S'_{AB} \neq S'_{BA}$, defining a four-dimensional feature vector

$$\vec{\Omega}(AB \neq BA) = \left\{ S'_{AA}\, S'_{AB}\, S'_{BA}\, S'_{BB} \right\}^T \tag{10a}$$

satisfying the normality condition which satisfies inherent energy and minimum phase conservation principles, where the norm of this vector satisfies the span-invariant

$$||\vec{\Omega}||^2 = Span\left\{ [\, S\,(AB \neq BA)\,] \right\} = |\, S'_{AA}\,|^2 + |S'_{AB}|^2 + |S'_{BA}|^2 + |S'_{BB}|^2 \tag{10b}$$

For the reciprocal monostatic (symmetric matrix) case, mainly considered here, the four-dimensional polarimetric feature vector mentioned above reduces to a three-dimensional feature vector because of $S'_{AB} = S'_{BA'}$, where

$$\vec{\Omega}(AB = BA) = \left\{ S'_{AA}\, \sqrt{2}\, S'_{AB}\, S'_{BB} \right\}^T \tag{11a}$$

satisfying the pertinent normality conditions

$$||\vec{\Omega}||^2 = Span\left\{ [\, S\,(AB = BA)\,] \right\} = |\, S_{AA}|^2 + 2|S_{AB}|^2 + |S_{BB}|^2 \tag{11b}$$

under a unitary basis transforming [21].
Note, that in the literature, formulations neglecting the multiplicative factor $\sqrt{2}$ exist [80] which are erroneous, because these formulations violate the energy and minimum phase conservation principles [20-22].
The corresponding correct polarimetric covariance matrices, [Σ(AB)] and [Σ(HV)], for the symmetric case, in the (AB) and (HV) bases, respectively, are then defined for the instantaneous state, respectively, by

$$[\Sigma(AB)] = \vec{\Omega}(AB)\vec{\Omega}(AB)^+ = \begin{pmatrix} S'_{AA} \\ \sqrt{2}\, S'_{AB} \\ S'_{BB} \end{pmatrix} (S'^*_{AA}\, \sqrt{2}\, S'^*_{AB} S'^*_{BB}) = \tag{12a}$$

$$= \begin{bmatrix} |\, S'_{AA}\,|^2 & \sqrt{2}\, S'_{AA}\, S'^*_{AB} & S'_{AA}\, S'^*_{BB} \\ \sqrt{2}\, S'_{AB}\, S'^*_{AA} & 2\,|\, S_{AB}\,|^2 & \sqrt{2}\, S'_{AB}\, S'^*_{BB} \\ S'_{BB}\, S'^*_{AA} & \sqrt{2}\, S'_{BB}\, S'^*_{AB} & |\, S'_{BB}\,|^2 \end{bmatrix}$$

and

$$[\Sigma(HV)] = \vec{\Omega}(HV)\vec{\Omega}(HV)^+ = \begin{pmatrix} S_{HH} \\ \sqrt{2} S_{HV} \\ S_{VV} \end{pmatrix} (S^*_{HH} \sqrt{2}\, S^*_{HV} S^*_{VV}) =$$

$$= \begin{bmatrix} |\, S_{HH}\,|^2 & \sqrt{2}\, S_{HH}\, S^*_{HV} & S_{HH}\, S^*_{VV} \\ \sqrt{2}\, S_{HV}\, S^*_{HH} & 2\,|\, S_{HV}\,|^2 & \sqrt{2}\, S_{HV}\, S^*_{VV} \\ S_{VV}\, S^*_{HH} & \sqrt{2}\, S_{VV}\, S^*_{HV} & |\, S_{VV}\,|^2 \end{bmatrix}$$

The 3x3 unitary transformation matrix [T] for transforming

$$\vec{\Omega}(AB) = [\, T\,]\, \vec{\Omega}(HV)$$

and (12b)

$$[\, \Sigma\,(AB)\,] = [\, T\,]\, [\, \Sigma\,(HV)\,]\, [\, T\,]^+$$

is then given, according to the definition of [T] and [U] of (97a,b) by

$$[\, T(\rho)\,] = \frac{1}{1 + \rho\, \rho^*} \tag{12c}$$

$$\begin{bmatrix} e^{2j\psi_1} & \sqrt{2}\, \rho\, e^{2j\psi_1} & \rho^2\, e^{2j\psi_1} \\ -\sqrt{2}\, \rho^*\, e^{j(\psi_1 + \psi_4)} & (1 - \rho\rho^*)\, e^{j(\psi_1 + \psi_4)} & \sqrt{2}\, \rho\, e^{j(\psi_1 + \psi_4)} \\ \rho^{*2}\, e^{2j\psi_4} & -\sqrt{2}\, \rho^*\, e^{2j\psi_4} & e^{2j\psi_4} \end{bmatrix}$$

where $[\, T(\rho)\,]\, [\, T(\rho)\,]^+ = [\, I\,]$ and $|\, Det\left\{ [\, T(\rho)\,] \right\}| = 1$ as is shown in [21].

2.2.2 Properties of the Polarimetric Covariance Feature Vector $\vec{\Omega}$ and Corresponding Covariance Matrix [Σ] for the Stochastic Monostatic Reciprocal (Symmetric) Case.

The recent availability of advanced coherent dual polarization radar systems allowing the decomposition of the received wave into two orthogonal components (co-polar and cross-polar transceiver channels), facilitated the introduction of the polarimetric feature vector $\vec{\Omega}$ of (12b) for interpreting the scattering behavior of reciprocal random targets ($S'_{AB} = S'_{BA}$). Utilizing the scattering matrix invariances of (10a/b), the polarimetric feature vector $\vec{\Omega}$ was introduced subject to the normality condition (12c), permitting the formulation of the covariance matrix [Σ] according to (13a/b) also for the stochastic symmetric case with < .. > = denoting either appropriate ensemble or time averaging of stochastic variables [20]

$$[\, \Sigma\,(AB)\,] = \tag{13a}$$

$$\begin{bmatrix} <|\, S'_{AA}\,|^2> & \sqrt{2} <S'_{AA}\, S'^*_{AB}> & <S'_{AA}\, S'^*_{BB}> \\ \sqrt{2} <S'_{AB}\, S'^*_{AA}> & 2<|\, S_{AB}\,|^2> & \sqrt{2} <S'_{AB}\, S'^*_{BB}> \\ <S'_{BB}\, S'^*_{AA}> & \sqrt{2} <S'_{BB}\, S'^*_{AB}> & <|\, S'_{BB}\,|^2> \end{bmatrix}$$

$$[\,\Sigma\,(HV)\,] = \tag{13b}$$
$$\begin{bmatrix} <|S_{HH}|^2> & \sqrt{2}<S_{HH}S_{HV}^*> & <S_{HH}S_{VV}^*> \\ \sqrt{2}<S_{HV}S_{HH}^*> & 2<|S_{HV}|^2> & \sqrt{2}<S_{HV}S_{VV}^*> \\ <S_{VV}S_{HH}^*> & \sqrt{2}<S_{VV}S_{HV}^*> & <|S_{VV}|^2> \end{bmatrix}$$

These polarimetric covariance matrices are directly related to the statistical properties of the scattering matrix elements and this proper formulation of [Σ] is also consistent with the Stokes reflection matrix decomposition into its co-polar matrix [M_c] and cross-polar matrix [M_x] as introduced in [9]. Following the approach of [6] and [11] of utilizing the reduced transformation matrix [4,6,11] with $\psi^1 = 0$ and $\psi^4 = 0$, equation (14a) may be reformulated as [21]

$$\vec{\Omega}\,(AB) = \vec{\Omega}\,(\rho) = [\,T\,(\rho)\,]\,\vec{\Omega}\,(HV) \tag{14a}$$

and

$$[\,\Sigma\,(AB)\,] = [\,\Sigma\,(\rho)\,] = <\vec{\Omega}\,(\rho)\,\vec{\Omega}^{+}\,(\rho)> = \\ = [\,T\,(\rho)\,]<\vec{\Omega}\,(HV)\,\vec{\Omega}\,(HV)>[\,T\,(\rho)\,] \tag{14b}$$

with

$$[\,T\,(\rho)\,] = \frac{1}{1+\rho\,\rho^*}\begin{bmatrix} 1 & \sqrt{2}\,\rho & \rho^2 \\ -\sqrt{2}\,\rho^* & (1-\rho\rho^*) & \sqrt{2}\,\rho \\ \rho^{*2} & -\sqrt{2}\,\rho^* & 1 \end{bmatrix} \tag{14c}$$

where $Det\{\,[\,T\,(\rho)\,]\,\} = 1$ and $[\,T\,(\rho)\,]\,[\,T\,(\rho)\,]^{+} = [\,I\,]$.
The particular form of [Σ (AB)] in (24) allows a reformulation in terms of the relevant normalized polarimetric co/cross-channel power expressions, $P_c\,(\rho)$ and $P_x\,(\rho)$, along the diagonal and the off-diagonal co-cross-polar-channel correlation (relative co-cross-polarization phase) expressions, $R_c\,(\rho)$ and $R_x\,(\rho)$, for the case of transmitting polarization state A and receiving B; whereas, for revised order of transmitting B and receiving A, the corresponding "orthogonal" expressions are denoted by $P_c\,(\rho)$, $P_x\,(\rho) = P_x\,(\rho)$ and $P_c\,(\rho) = R_c\,(\rho)$ and $P_x\,(\rho)$, where [20]

$$[\,\Sigma\,(\rho)\,] = \begin{bmatrix} P_c\,(\rho) & \sqrt{2}\,R_x\,(\rho) & R_c\,(\rho) \\ -\sqrt{2}\,R_x\,(\rho)^* & 2\,P_x\,(\rho) & \sqrt{2}\,R_x\,(\rho)^* \\ R_c\,(\rho)^* & \sqrt{2}\,R_x\,(\rho) & P_c\,(\rho) \end{bmatrix} \tag{15a}$$

and since $\rho\,\rho^* = -1$, and the covariance matrix is Hermitian, we find

$$\left[\,\Sigma\left(\rho = -\frac{1}{\rho^*}\right)\right] = \tag{15b}$$
$$= \begin{bmatrix} P_c\,(\rho) & \frac{-\rho}{\rho^*}\sqrt{2}\,R_x\,(\rho) & \frac{\rho^2}{\rho^{*2}}R_c\,(\rho)^* \\ \frac{-\rho^*}{\rho}\sqrt{2}\,R_x\,(\rho)^* & 2\,P_x\,(\rho) & \frac{-\rho}{\rho^*}\sqrt{2}\,R_x\,(\rho)^* \\ \frac{\rho^{*2}}{\rho^2}R_c\,(\rho)^* & \frac{-\rho^*}{\rho}\sqrt{2}\,R_x\,(\rho) & P_c\,(\rho) \end{bmatrix}$$

satisfying the following orthogonality relations

$$P_c\left(-\frac{1}{\rho^*}\right) = P_c\,(\rho) \tag{15c}$$

$$\left|\,R_x\left(-\frac{1}{\rho^*}\right)\right| = \left|\,R_x\,(\rho)\,\right| \tag{15d}$$

and symmetry relations

$$P_x\left(-\frac{1}{\rho^*}\right) = P_x\,(\rho) \tag{15e}$$

$$\left|\,R_c\left(-\frac{1}{\rho^*}\right)\right| = \left|\,R_c\,(\rho)\,\right| \tag{15f}$$

Using above expressions, the stochasticity coefficients, defined in (17c) to (17e), may be reformulated as [21]

$$\mu_{AB}\,(\rho) = \frac{R_x\,(\rho)}{\left\{P_c\,(\rho)\,P_x\,(\rho)\right\}^{1/2}} \tag{15g}$$

and

$$q_{AB}\,(\rho) = \frac{\left\{(P_c\,(\rho) - P_x\,(\rho))^2 + 4\,|\,R_x\,(\rho)\,|^2\right\}^{1/2}}{\left\{P_c\,(\rho) + P_x\,(\rho)\right\}} \tag{15h}$$

with

$0 \le |\,\mu_{AB}\,(\rho)\,| \le q_{AB}\,(\rho)\,1 \le 1$.

As summarized by Lüneburg et al. [74] and in [21], the covariance matrix [Σ] is Hermitian and positive semi-definite (three real diagonal power terms and three complex cross-correlations) [44] and thus possesses three real, non-negative eigenvalues $0 \le \nu_1 \le \nu_2 \le \nu_3$ corresponding to a given matrix [Σ] or equivalently [M], i.e., ν_i ([M], i = 1,2,3), where it can be shown that

$$0 \le \nu_1 \le \min_\rho P_c\,(\rho) \le P_c\,(HV) \le \max_\rho P_c(\rho) \le \nu_3 \le |\,|\vec{\Omega}(HV)|\,|^2 \tag{16a}$$

and similar inequalities hold for P_c and P_x. A succinct interpretation of the target invariant eigenvalues ν_i (1,2,3) of the covariance matrix on random target polarimetric backscattering features is summarized in [20,71], showing that the smallest eigenvalue ν_1 indicates the degree of randomness. For a deterministic target, with the covariance matrix defined by (12) as $[\,\Sigma\,(HV) = \vec{\Omega}\,(HV)\,\vec{\Omega}^{+}\,(HV)$, one obtains by involving a spectral theorem of matrix algebra [44] that $\nu_1 = \nu_2 = 0$ and $\nu_3 = |\,|\,\vec{\Omega}\,(HV)\,|\,|^2$ for which true null polarization states $\rho_{cn1,2}$ exist [21,74]. The eigenvalue difference $\Delta\,\nu = (\nu_{max} - \nu_{min}) = (\nu_3 - \nu_1)$ of extremal covariance matrix eigenvalues determines the range in which the mean power return $P_c\,(\rho)$ and $2P_x\,(\rho)$ can be varied by polarimetric transceiver antenna adjustments, where in particular

$$Trace\{[\Sigma(AB)]\} = Trace\{[\Sigma(HV)]\} =$$
$$= Trace\{<\vec{\Omega}\vec{\Omega}^{+}>\} = <Trace\{\vec{\Omega}\vec{\Omega}^{+}\}> =$$
$$<||\vec{\Omega}||^2> = <Span\{[S]\}> = <|S_{AA}|^2> =$$
$$= +2<|S_{AB}|^2> + <|S_{BB}|^2> =$$
$$<|S_{HH}|^2> + 2<|S_{HV}|^2 + <|S_{VV}|^2> =$$
$$= \nu_1([\Sigma]) + \nu_2([\Sigma]) + \nu_3([\Sigma]) = \textit{invariant} \quad (16b)$$

Additionally, the span of the covariance matrix [Σ] is also an invariant [44], where

$$Span\{[\Sigma]\} = \sum_{i=1}^{3} \nu_i^2 = \textit{invariant} \quad (16c)$$

and so is the ratio of the span versus the trace of the covariance matrix [Σ] an invariant such that the '**covariance matrix invariance ratio (cmir)**' may be defined as [21]

$$'cmir' = \frac{(Span\{[\Sigma]\})^{1/2}}{Trace\{[\Sigma]\}} = \frac{(Span\{[\Sigma]\})^{1/2}}{Trace\{[\Sigma]\}} = \frac{\left(\sum_{i=1}^{3} \nu_i^2\right)^{1/2}}{\sum_{i=1}^{3} \nu_i} =$$
$$= \textit{invariant} \quad (16d)$$

In POL-RAD/SAR signal and image processing 'cmir' plays a major role specifically as a measure (standard) for speckle reduction.

Similar definitions are used to derive an optimal image from the complex elements HH, HV, and VV of [S] specifically by MIT-LL/EML group [80] for the reciprocal backscattering case. If, for instance, the ratio of the standard deviation is taken as a measure of image optimization, i.e., of speckle reduction, such that

$$\frac{S}{M} = \frac{st.\,dev.\{y\}}{E\{y\}} \quad (17a)$$

where the random variable y denotes pixel intensity, then the random variable y for each image element (pixel) is given by

$$y = \vec{X}^{T}[C]\vec{X} \quad (17b)$$

where the 3x3 matrix [C] was formulated to be Hermitian symmetric and positive definite and is called the Optimal Weighting Matrix. The determinant of the elements C_{is} of [C] can be associated by those of the 3x3 Covariance Matrix [Σ] of (25) which requires further subtle analysis. This eigenvalue problem needs to be solved for pixel intensities of a given image having the minimum possible standard deviation-to-mean ratio.

In order to determine the Optimal Weighting Matrix [C] (i.e., the matrix that results in an image whose pixel intensities have a minimum possible standard deviation-to-mean ratio), the following statistical methods can be used:

$$E\{y\} = Tr\left(\sum\nolimits_{c}[C]\right) = \sum_{i=1}^{3} \lambda_i \quad (17c)$$

$$Var\{y\} = Tr\left(\sum\nolimits_{c}[C]\right)^2 = \sum_{i=1}^{3} \lambda_i^2$$

where $\lambda_1, \lambda_2, \lambda_3$ are the eigenvalues of the matrix $\Sigma_c[C]$. Then the ratio becomes

$$\frac{S}{M} = \frac{\sqrt{\sum_{i=1}^{3} \lambda_i^2}}{\sum_{i=1}^{3} \lambda_i} \quad (17d)$$

Therefore, the optimal weighting matrix [C] is one that yields eigenvalues $\lambda_1, \lambda_2, \lambda_3$ that minimize the s/m ratio and it provides a close affinity with the definition of 'cmir' given by (16c).

These covariance matrix approaches of the MIT-LL/EML groups, when corrected to satisfy basic principles of energy conservation, as shown by Lüneburg et al. [74] and Boerner et al. [21], may provide a satisfactory method which incorporates both solutions to Maxwell's equations as well as rigorous electromagnetic/statistical principles developed in communications, estimation and signal detection theory [45]. It is interesting to note that in the rigorous and exact (corrected) covariance matrix approach, presented and developed by Lüneburg et al. [74] and Boerner et al. [21], which is consistent with the optimization procedures for determining the Kennaugh and Huynen target characteristic polarization state theories [20], an expression similar to (16) is obtained which related the span versus trace to the correctly defined 'cmir', given by (26d), where ν_i are the eigenvalues of [Σ]. Because polarimetric radar theory is based on the exact Maxwell equations formulation, instead of only pursuing statistical image processing methods, a more rigorous basic approach is still required.

2.3 Optimal Speckle Reduction vs. Image Discrimination

A comparison of scalar filtering methods, the statistical standard deviation/mean method and the polarization matched filter method.

2.3.1 Speckle Reduction through Filtering

Image filters are scalar (i.e. not polarimetric or complex-valued) enhancement methods for digital images which are used for pattern recognition, smoothing, sharpening and weighting of digital image points [4,5,75,76]. A typical image filter of this type applies a weight operator to every pixel of an image area in order to emphasize or suppress certain information. As a rule, selected filters are chosen by the users, based on their visual preferences and ability to interpret the optical information. This trial-and-error approach does not lend itself to automation, especially when dealing with such complex phenomena as speckle or periodic noise. Smoothing, i.e. Fourier transforming, is one of the most common methods used to remove periodic noise or speckle, if it can be isolated and canceled out in the Fourier domain [30,83,84]. If noise is multiplicative (homomorphic), however, undesirable frequency components cannot be isolated so easily. In any event, speckle reduction through filtering requires a great deal of interactive intervention by a user.

2.3.2 Speckle Reduction through Optimal Detection Performance

Given the large number of data (pixels) in an image and assuming that their random distribution is approximately Gaussian, the following methods have been developed to deal with complex-valued POL-SAR image data in the form of the complex scattering matrix [S] or its associated Mueller matrix [M].
The ratio of the standard deviation versus the mean is taken as a measure of image optimization, i.e. speckle reduction. An optimal weighting matrix is applied to every pixel to minimize the standard deviation/mean ratio.

2.3.3 Speckle Reduction through the Polarimetric Matched Filter Method

In this method the approach is taken, that poor image quality, including noise and speckle, is related to a mismatch between the polarization states of the sending and receiving antennas. The complex image data are statistically evaluated and the 'receiving antenna' is mathematically fine-tuned (i.e. rotated) which may results in an increase in image contrast between different regions of reflectivity (roughness of terrain such as ocean, buildings, and vegetated terrain). Another major benefit of this method is a reduction in noise and speckle which either disappears when the receiving or transmitting antenna is rotated to a different polarization state or can be identified by comparing and subtracting two of the same images, received at different polarization states.

2.3.4 Usefulness of these Methods in Automated Applications

- Application of well-formulated, advanced mathematical treatment for image enhancement, pattern recognition, computer-based image evaluation;
- Data are prepared for image evaluation through proper histogramming, simplifying subsequent computer-processing tasks and resulting in verifiable, not subjective outcomes.
- In the PMIF method, for instance, since a rotation of the receiving or transmitting antennas can be simulated electronically, incidents of measurement errors due to equipment faults, irregularities or deviations from original flight path (if it needs to be flown again), etc. are reduced to a minimum.
- Characteristic signatures of specific surface structures or events (such as ocean, buildings, vegetated areas, moving objects, etc.) are easily identified without the need of human interpretation.

2.4 Summary

So far, we have presented two useful groups of methods of image enhancement and speckle reduction, namely the widely used "classical" computer-numerical image enhancement methods of section 2.1, and a speckle and noise suppression method through statistical averaging of the scattering matrix elements in section 2.2. Although these methods offer some speckle reduction and a limited possibility of automation, we are interested in this paper on a new approach in POL-SAR image analysis which analyses the given complex-valued, coherent polarization data from a more desirable viewpoint which comes closer to electromagnetic vector wave theory.
Since the POL-SAR data are provided in the 2x2 Sinclair or 4x4 Mueller scattering matrix format which contains all the polarization transformation information of the reflected EM wave after its interaction with terrain/clutter. In the following PMIF method which was developed by Boerner, Kostinski, James et al. [16-22,63-67], the polarization orientations of the receiving or transmitting antennas of the POL-SAR system are simulated in the computer and matched polarimetrically to a given data set in order to enhance the features of an image and to reduce unwanted noise and speckle, among other things.

3. A FIRST ORDER POLARIZATION ADJUSTMENT PROCEDURE FOR SAR IMAGERY

3.1 Inclusion of Polarization Information in SAR Images

Polarization-agile SAR provides coherent magnitude and phase data of the co- and cross-polarized scattering matrix elements on a pixel-by-pixel basis, i.e. every pixel of the image consists of eight unique parameters. Since various terrains or targets respond to one polarization state more than to others, an incident polarization could be chosen to enhance the response of one type of terrain (target) while suppressing, i.e. not using a preferred polarization state, for objects or background within the image region. Furthermore, by tuning the receiver antenna polarization state such that the incoming scattered wave can either be suppressed or completely received by properly matching the signals during image processing.
One method which will accomplish this task is called the Polarization Matched Image Filter (PMIF). The PMIF has the following characteristics:

- it offers the freedom of changing the transmitted or received polarization states in a post-processing mode, assuming that the scattering matrix elements are measured and calibrated correctly, i.e., are pure target-characteristic parameters and will not depend on antenna polarization characteristics, propagation path distortions, etc;

- the PMIF can be used as an adjustable tuner (filter) to transmit or receive a desirable polarization which will enhance a specific target feature such as ships or other man-made objects or ocean wave patterns, etc., in an adaptive post-processing mode. Optimal performance of the PMIF is based on a statistical evaluation prior to the imaging/graphics process. The PMIF method described here reduces human intervention during the decision process which is a first step toward automation; and it also allows for complete polarimetric matching to a known desirable scatterer (target) versus undesirable scatterers (targets), where the scattering matrix can be modelled in advance; thus rendering the "Polarimetric Matched Filtering" method feasible.

This approach was first proposed by Boerner [13] and a feasibility study was conducted at Honeywell DSD, Twin Cities, MS during 1982-86, and then the approach was further pursued within UIC-EECS/CL [60-64].

3.2 The Limited Polarization Matched Image Filter Approach Using [G]

A polarimetric matched filter technique [63-67] was developed to increase image contrast between terrain classes and to reduce speckle by readjusting transmitting and receiving antennas. This polarization matched filter technique conducts a search for an optimal desirable (statistically most popular) polarization state of an image patch, i.e. finding such transmitting and receiving polarizations that the received power is at a maximum, where $P \equiv |V^* V|^2 = (\vec{h}^T \vec{E_R})^* (\vec{h}^T \vec{E_R})$, where V stands for the voltage at the receiving antenna as a function of transmitter/target/receiver polarizations and $\vec{h}$ is the antenna height (i.e. the polarization state of receiving antenna when transmitting). Hence, the purpose of this procedure is to determine such $\vec{E_T}$ and $\vec{h}$, that the voltage equation

$$V = \vec{h}^t \vec{E_R} = \vec{h}^t [S] \vec{E_T} \tag{18}$$

is optimal for a given [S], subject to the constraints and $||\vec{h}|| = ||\vec{E_T}|| = 1$ (which actually implies 'norm'-averaging in the sense of gray-scale normalization).

3.3 The Limited Power Match Procedure of the Graves Power Matrix [G]:

The Three-Stage Procedure (TSP)
The TSP uses the scattering matrix of a target (pixel) and calculates the received power, i.e. P_w of the scattered wave is $\vec{E_R}^t \vec{E_R}$; $^t \equiv (^*)^T \rightarrow$ Hermitian conjugate. Hence,

$$P_W = \vec{E_R}^t \vec{E_R} = ([S] \vec{E_T})^t [S] \vec{E_T} = \vec{E}^t [S]^t [S] \vec{E_T} \equiv \vec{E_T}^t [G] \vec{E_T} \tag{19}$$

assuming that $\vec{E_R} = [S] \vec{E_T}$, where ^{T} implies the transpose of the argument.
Since the complex Graves power matrix [G] is defined as $[S]^T [S]$, which is a Hermitian matrix for any [S], it is of interest to maximize P_w to find the "best" $\vec{E_T}$ for a given target. The form containing [G] is known as a positive definite matrix which is defined as $x^T \underline{\underline{A}}\, x > 0$ for all non-zero vectors $\vec{x}$, with $\vec{x_i}$ being the corresponding unit eigenvector, where

$$[A] \vec{x_i} = \lambda_i \vec{x_i} \text{ and } \vec{x_i}^T [A] \vec{x_i} = \vec{x_i}^T \vec{\lambda_i}^T \lambda_i \vec{x_i} = \lambda_i \tag{20}$$

Since $\vec{x_i}^T \vec{x_i} = 1$ and the quantity $\vec{x_i}^T [A] \vec{x_i} = \lambda$ is a positive eigenvalue. Assuming that all $\lambda_i > 0$, then all $\vec{x}^T [A] \vec{x} > 0$.
Also, the determinant of any matrix is the product of its eigenvalues, so that

$$Det\,[A] = \lambda_1 \lambda_2 \ldots \lambda_n > 0 \tag{21a}$$

and the trace is the summation of those elements

$$tr\,[A] = \lambda_1 + \lambda_2 + \ldots \lambda_n > 0 \tag{21b}$$

$[A]\vec{x} = \lambda \vec{x}$ is the fundamental equation for the eigenvalue λ and the eigenvector $\vec{x}$. It is non-linear, because it involves the product of both unknowns λ and $\vec{x}$. Finding λ would mean that the equation with just the vector $\vec{x}$ becomes linear. Furthermore, if $\lambda \vec{x}$ is replaced by $\lambda I \vec{x}$, then

$$[A]\vec{x} = \lambda [I]\vec{x} \; or \; ([A] - \lambda [I])\vec{x} = 0 \tag{22}$$

The final step of this mathematical development involves the use of the Rayleigh quotient

$$R(x) = \frac{\vec{x}^T [A] \vec{x}}{\vec{x}^T \vec{x}}, \tag{23}$$

because solving $[A]\vec{x} = \lambda \vec{x}$ is equivalent to minimizing R(x). Applied to the power expression of Hermitian form

$$\vec{x}^t [G] \vec{x} / \vec{x}^t \vec{x} \tag{24}$$

and assuming that the eigenvalues are real and orthonormal, the following two equations (18a,b) can be used to find the eigenvalues:

$$Det\{[G]\} \equiv g_{11} g_{22} - g_{12} g_{21} = \lambda_1 \lambda_2 = Det\{[S]\} Det\{[S]^*\} \tag{25}$$

$$tr\{[G]\} \equiv g_{11} g_{22} = \lambda_1 + \lambda_2 = Span\{[S]\}, \tag{26}$$

with σ_0 = Span $\{[S]\} + 2\,|Det\{[S]\}$ representing the effective cross-section, σ_0, of a radar target according to Kennaugh [59].
After substituting and rearranging,

$$Det\{[G]\} = \lambda_1 [tr\{[G]\}] - \lambda_1^2 \tag{27}$$

and solving for λ gives:

$$\lambda_{1,2} = \frac{tr\{[G]\} \pm [(tr\{[G]\})^2 - 4\det\{[G]\}]^{1/2}}{2} \tag{28}$$

which are the eigenvalues of interest here purposefully expressed in terms of the intrinsic invariants, the Span {[S]} and Det {[S]}. Using these eigenvalues, $\lambda_{1,2}$ in the power equation, the extremum is obtained if the vector, $\vec{E}_T$ satisfies the following eigenvalue equation:

$$\{[G] - \lambda [I]\} E_{T,opt} = 0 \tag{29}$$

This eigenvector, $\vec{E}_{T,opt}$, corresponding to the greatest power flux density of the transmitted field. The eigenvector, found by substituting the smaller eigenvalue, corresponds to the lowest power flux density of the transmitted field and is orthogonal due to the fact that [G] is hermitian.

The second eigenvector can also be found by using the orthogonality condition

$$\vec{E}^1_{T,opt} + \vec{E}^2_{T,opt} = 0 \tag{30}$$

Stage 2 of the TSP uses the eigenvectors such that the power of the scattered wave is maximized which is done by simply substituting $\vec{E}_{T,opt}$ into the equation:

$$\vec{E}_{R,opt} = [S]\vec{E}_{T,opt} \tag{31}$$

Generally, $\vec{E}_{R,opt} \neq \vec{E}_{T,opt}$ since $[S]^T [S] \neq [S][S]^t$ except for normal matrices [S] which, however, are dominant.
The third stage of the TSP involves an adjustment of the receiver polarization to match the polarization state of the scattered wave. Here, the notion of antenna height plays the role of adjusting the receiving antenna to receive maximum scattered power by taking into consideration the corresponding transmit polarization it would have had to use as a transmitting antenna, such that:

$$\vec{h} = \frac{\vec{E}_R^*}{||\vec{E}_R||} \; or \; \vec{h}_{opt} = \frac{[S]\vec{E}^*_{T,opt}}{||[S]\vec{E}_{T,opt}||} \tag{32}$$

where, $||\;||$ corresponds to the norm and the complex conjugation suggests the reversal of the sense of rotation of the polarization ellipse upon scattering, which is significant in terms of polarization matching the antennas. Note, that a complete polarization mismatch can be found as well which is quite useful when wanting to eliminate certain prominent polarization states while enhancing others, e.g., reject the most "popular" ocean clutter polarization state of an ocean image patch in order to enhance non-ocean-like objects in that patch such as one with ships. Therefore, a complete polarization match is accomplished by choosing $\vec{h} = \vec{E}_R^*$ and a mismatch requires that $V = \vec{h}^T \bullet \vec{E}_R = 0$. However, by inflicting the complex conjugated matching condition, the degree of freedom of polarimetrically adjusting the image information is reduced substantially; and therefore, in the next Section 3.4 the "complete coherent polarization fork operator approach is presented [19].
The following chart (Fig. 3.1) and Fig. 3.2 show the TSP procedure in the form of a flow chart where the arrows point out the sequence of events and Figs 3.2a, b, c show the results.

3.4 PMIF Application to the CV 990 SAR Data Set - Results of PMIF Processing

The three images of Figure 3.2 show how the PMIF method suppresses unwanted ocean clutter by increasing the contrast between ocean-like and city-like image fea-

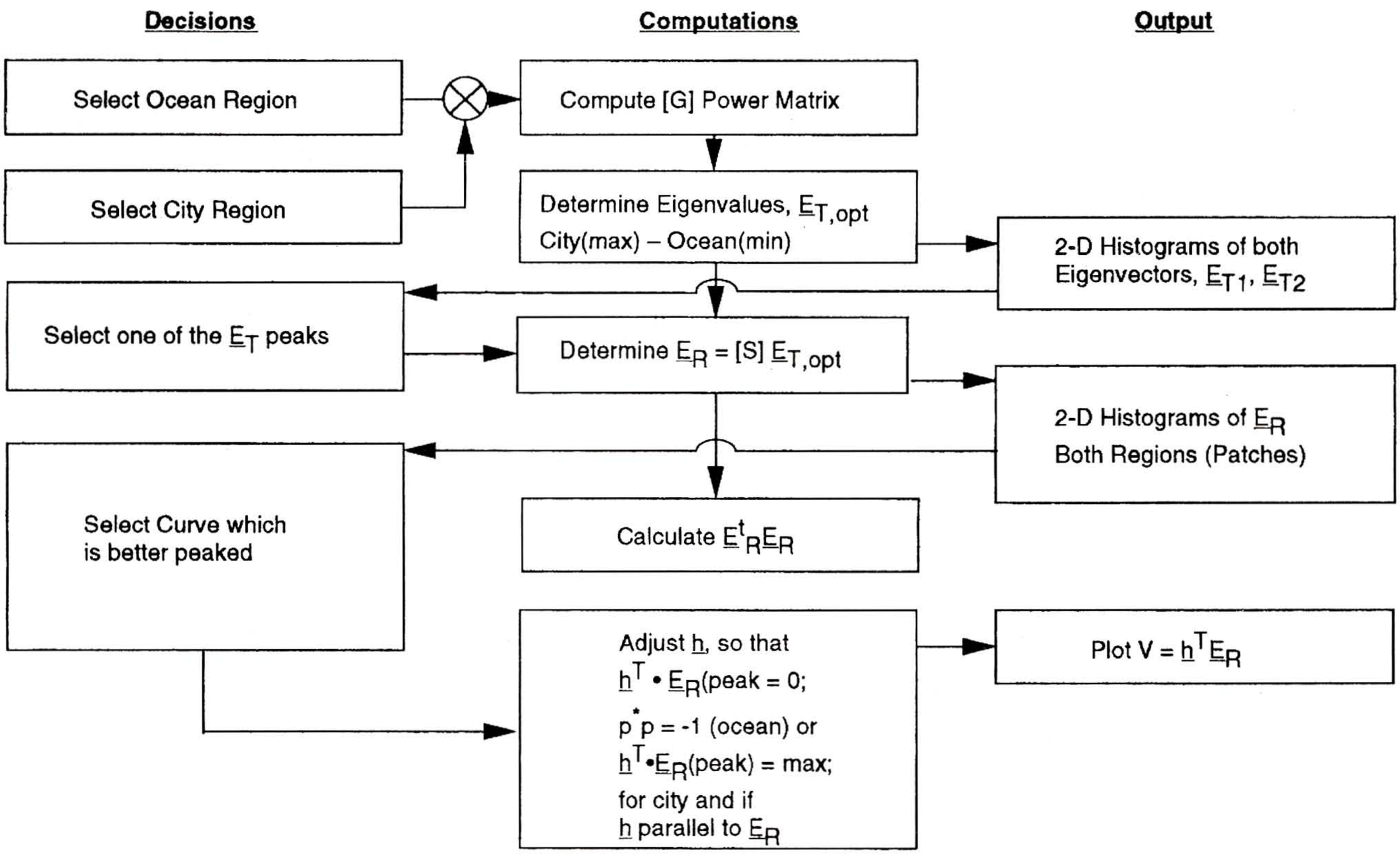

Fig. 3.1 - Flow Chart PMIF with Applications to Ocean/City Contrasting.

tures in terms of their most favorable polarizations. The HH-magnitude and span images show a lot of speckle and ships in the ocean cannot be differentiated easily from ocean clutter. The following two PDFs show the joint distributions of optimal polarizations for the selected ocean and city regions. The eigenvectors, which were computed over the ocean and city regions, according to step 1 of the PMIF, were histogrammed in their ellipticity and tilt parameters. The eigenvectors of the ocean region correspond to minimization of the energy density in the reflected field. It can be seen that the majority of backscattered energy is received at 0° ellipticity and 90° tilt, while the city region has peaks at the same ellipticity but tilts at 90° as well as 0°. Hence, the polarization ellipse with ellipticity of 0° and tilt of 0° will mismatch the ocean but match the city so that city-like, i.e. man-made angular structures, will be contrasted strongly against the ocean.
It should be noted that the proper polarization adjustment of the filter depends primarily on the correct selection of the tilt value since the range of the ellipticity is quite narrow. This sensitivity to tilt, i.e. phase, however, makes this procedure extremely vulnerable to phase and calibration errors during measurements [118].

4. THE GENERALIZED POLARIMETRIC MATCHED IMAGE FILTER [123]

With this method all existing characteristic states can be determined for which the radar receiver obtains maximum/minimum power scattered back from the targets and for which optimum polarization phase (δ) instabilities may occur (21, 118, 123-125]. The receiver power, expressed as

$$P_R = |V_R|^2 = V_R^* V_R \tag{33}$$

can be rewritten as

$$P = |V|^2 = |\vec{E}_R{}'^T [S] \vec{e}|^2 ; \ \vec{e} = \vec{E}/||\vec{E}|| = \vec{E}_R{}'^T [S'] \vec{e}_T{}' |^2 \tag{34}$$

where (′) represents the reference to any new basis (AB) which is obtained after the unitary transformation from the original basis (HV) [1,26,63,123-125].
In mathematics, the maximum and minimum of a function can be found at the critical points of the function. Here, we apply the critical point method to the power function (40). A more direct way of doing so is by diagonalizing

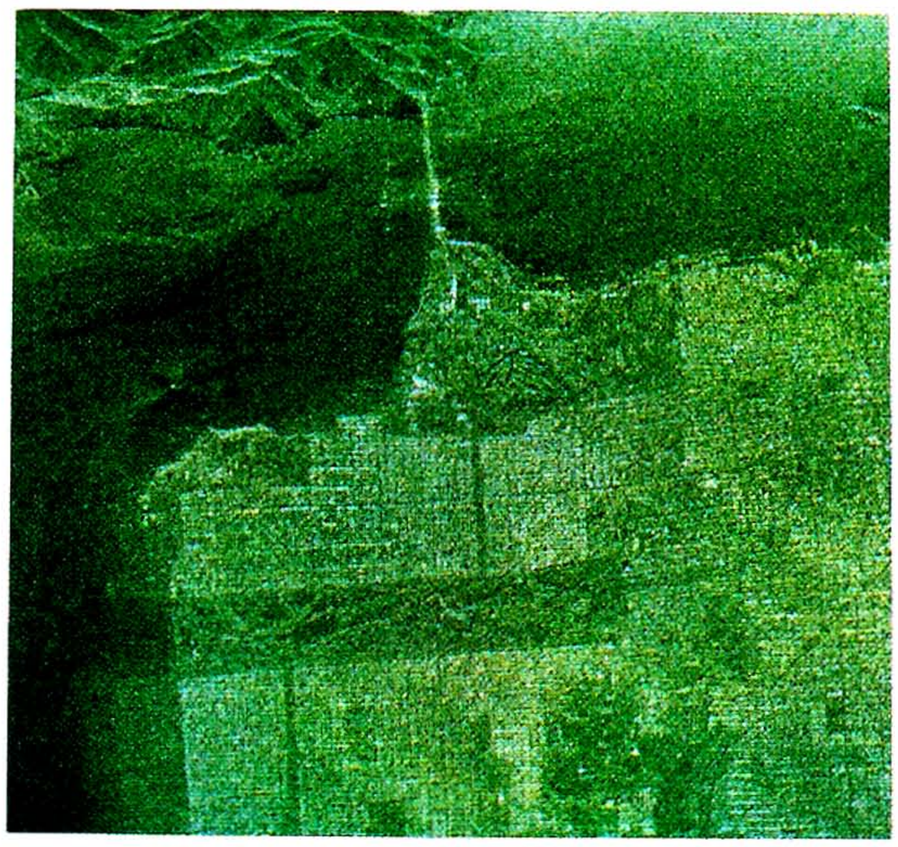

(a)

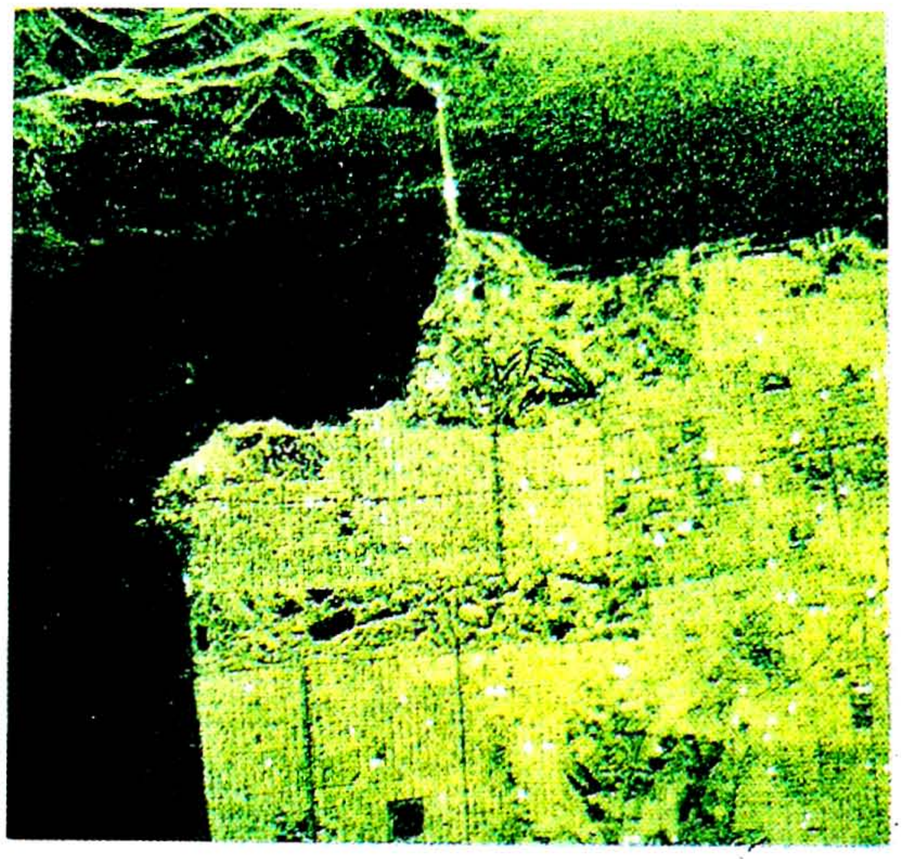

(b)

(c)

Fig. 3.2 - Comparison between: (a) HH-Magnitude, (b) Span, and (c) PMIF Image.

the scattering matrix [S] in function (40) by implementing the unitary transformation, i.e., let

$$[\,S'\,(AB)\,] = \begin{bmatrix} S'_{AA} & S'_{AB} \\ S'_{BA} & S'_{BB} \end{bmatrix} = [\,U\,]^T \begin{bmatrix} S_{HH} & S_{HV} \\ S_{VH} & S_{VV} \end{bmatrix} [\,U\,] \quad (35)$$

where $S_{HV} = S_{VH}$ and $S_{AB}' = S_{BA}'$ for the monostatic scattering case [19,122].

To diagonalize that scattering matrix $[\,S'\,(AB)\,]$, we let $S_{AB}' = 0$ and find the diagonalization factor [1,122] $\rho_{1,2}$ as:

$$\rho_{1,2} = \frac{-B \pm \sqrt{B^2 - 4AC}}{2A} = |\,\rho_{1,2}\,|\, e^{j\,\delta_{1,2}} \quad (36)$$

where

$A = S_{HH}^{\,*}\, S_{HV} + S_{HV}^{\,*}\, S_{VV}$, $B = |\,S_{HH}\,|^2 - |\,S_{VV}\,|^2$, $C = -A^*$

Therefore, that scattering matrix is in diagonal form

$$[\,S'\,(AB)\,] = \begin{bmatrix} S'_{AA} & 0 \\ 0 & S'_{BB} \end{bmatrix} = \begin{bmatrix} \lambda_1 & 0 \\ 0 & \lambda_2 \end{bmatrix} = [\,S_d\,] \quad (37)$$

with

$$\lambda_1 = S'_{AA}\,(\rho_1) = (1+\rho_1\,\rho_1^*)^{-1}\,(S_{HH}+2\rho_1\,S_{HV}+\rho_1^2\,S_{VV})\,e^{2j\,\Psi_1} = |\,\lambda_1\,|\,e^{j\,\phi_1} \quad (38a)$$

$$\lambda_2 = S'_{BB}\,(\rho_1) = (1+\rho_1\,\rho_1^*)^{-1}\,(\rho_1^{*2}\,S_{HH}+2\rho_1^*\,S_{HV}+S_{VV})\,e^{2j\,\Psi_4} = |\,\lambda_2\,|\,e^{j\,\phi_2} \quad (38b)$$

The function of the power return to the co-pol and cross-pol channels of the receiver are determined from the bilinear form (40) to become:

(i) For the function of the power returned to the cross-pol channel ($\vec{E_R} = \vec{E_T}$)

$$P_x = |V_x|^2 = |h'^T [S_d] h'|^2 = (1 + \rho' \rho'^*)^{-2} \quad (39)$$
$$(|\lambda_1|^2 \rho' \rho'^* - \lambda_1 \lambda_2 \rho'^{*2} - \lambda_1^* \lambda_2 \rho'^2 + |\lambda_2|^2 \rho' \rho'^*)$$

where ρ' is the polarization ratio of the receiver in the new basis. The critical points are some ρ' *s* with the first derivative of P_x with respect to ρ' and ρ'^* vanishes. These critical points, found in function P_x, are:

$$\rho'_{xn1} = 0 \quad (40a)$$

$$\rho'_{xn2} = \infty \quad (40b)$$

$$\rho'_{xm1,2} = \pm i \left(\frac{\lambda_1 \lambda_2^*}{\lambda_1^* \lambda_2} \right)^{1/4} = \pm e^{j(2\nu + \pi/2)} \quad (40c)$$

$$\rho'_{xs1,2} = \pm \left(\frac{\lambda_1 \lambda_2^*}{\lambda_1^* \lambda_2} \right)^{1/4} = \pm e^{j2\nu} \quad (40d)$$

(ii) For the function of the power returned to the co-pol channel ($\vec{E_R} = \vec{E_T}$)

$$P_c = |V_c|^2 = |h'^T [S_d] h'|^2 = (1 + \rho' \rho'^*)^{-2} \quad (41)$$
$$(|\lambda_1|^2 + \lambda_1 \lambda_2^* \rho'^{*2} + \lambda_1^* \lambda_2 \rho'^2 + |\lambda_2|^2 \rho'^2 \rho'^{*2})$$

the critical points are determined from

$$\rho'_{cm1} = \rho'_{xn1} = 0\,, \quad \rho'_{cm2} = \rho'_{xn2} = \infty\,, \quad (42a,b)$$

$$\rho'_{cn1,2} = \pm \left(-\frac{\lambda_1}{\lambda_2} \right) = \pm \left(\frac{|\lambda_1|}{|\lambda_2|} \right)^{1/2} e^{j(2\nu + \pi/2)} \quad (42c)$$

Note, that the following conditions are satisfied [122]

$$\rho'_{xn1} \rho'^*_{xn2} = -1 \quad (43a)$$

$$\rho'_{xm1} \rho'^*_{xm2} = -1 \quad (43b)$$

$$\rho'_{xs1} \rho'^*_{xs2} = -1 \quad (43c)$$

that means that not only ρ'_{xn1} and ρ'_{xn2} but also ρ'_{xm1} and ρ'_{xm2} are orthogonal and so are ρ'_{xs1} and ρ'_{xs2}.

4.1 X-POL Null and Co-Pol Maximum States

It can be shown for the monostatic reciprocal case that the X-Pol Nulls and the CO-POL Maxima are identical as shown in (49a,b).
The power return to the cross/co-pol channels are [122]

$$P_{xn1}(\rho'_{xn1}) = P'_{xn2}(\rho'_{xn2}) = 0 \quad (44a)$$

$$P_{co1}(\rho'_{cm1} = |\lambda_1|^2 \quad (44b)$$

$$P_{co2}(\rho'_{cm2} = |\lambda_2|^2 \quad (44c)$$

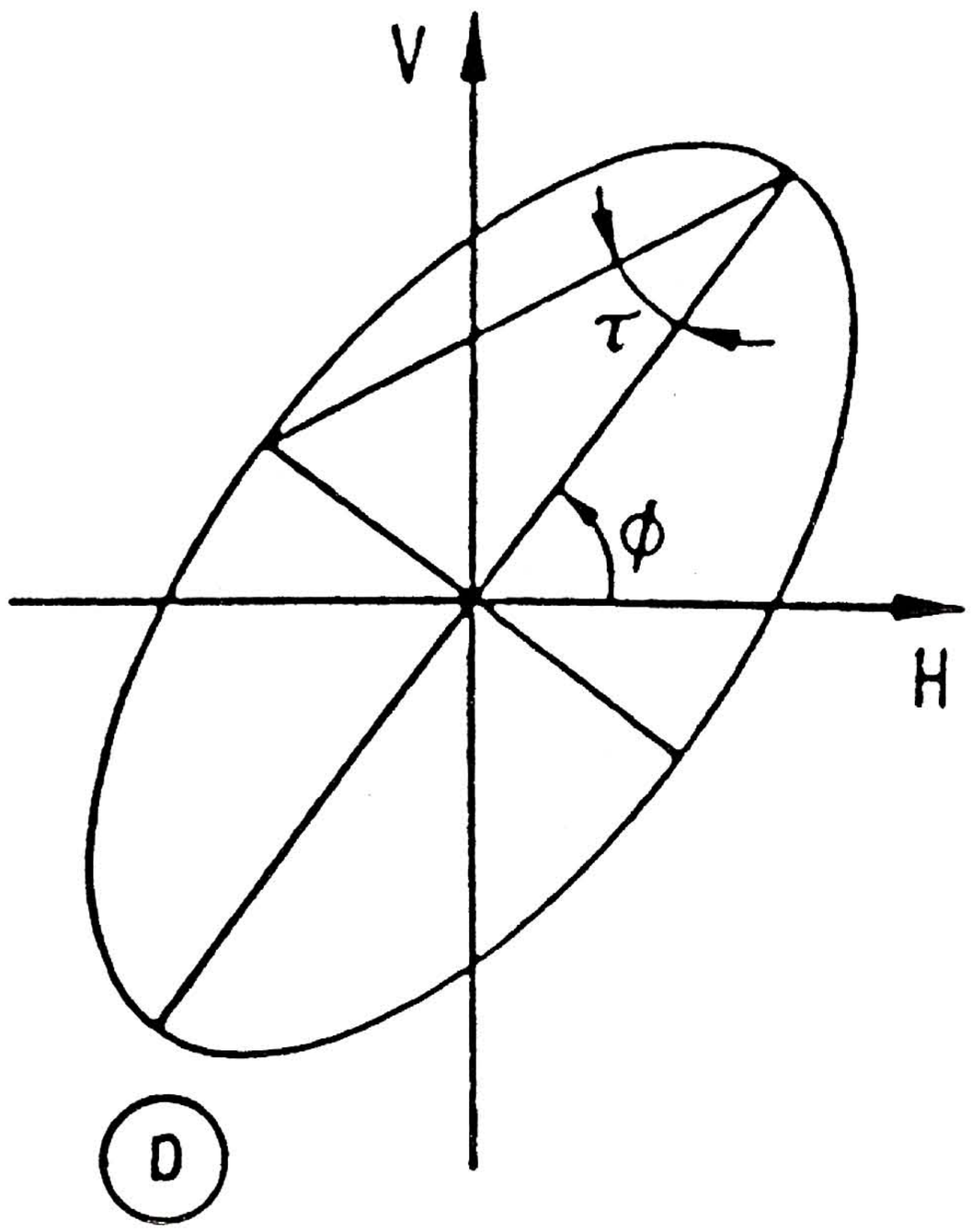

Fig. 4.1a - Parametric presentation of the polarization ellipse.

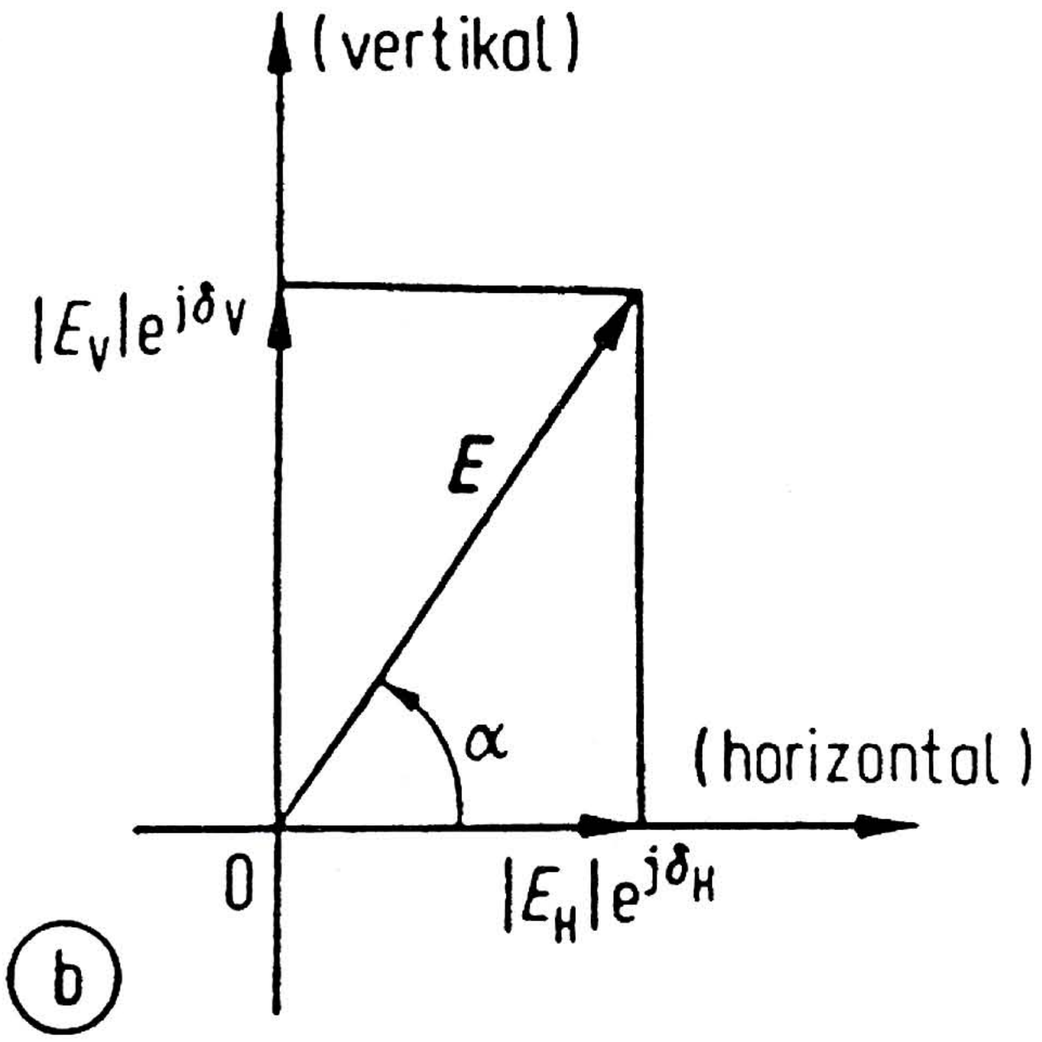

Fig. 4.1b - Representation of the polarization ratio in the horizontal-vertical (H-V) basis.

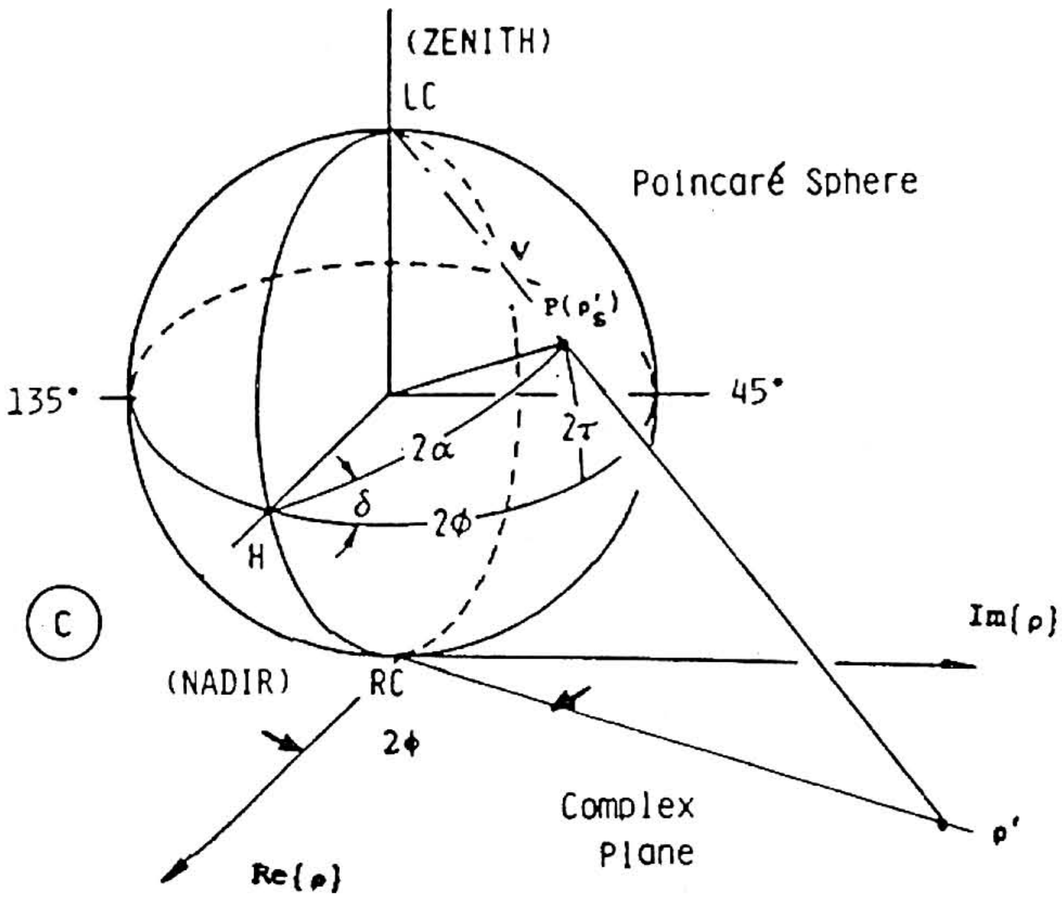

Fig. 4.1c - Representation of a polarization state on the Poincaré sphere with correspondence of point on the complex polar plane, ρ′, with point P (ρ′s) on the polarization sphere.

4.2 CO-POL Nulls, X-POL Maxima, and X-POL Saddles

The $\rho'_{xm1,2}$ of (52c) are the cross-pol maxima and $\rho'_{xs1,2}$ of (52d) are the cross-pol saddles. The corresponding power returns to the receiver of the cross-co-pol channels are:

$$P_x(\rho'_{xm1,2}) = 1/4\,(\,|\lambda_1| + |\lambda_2|\,)^2 \tag{45a}$$

$$P_c(\rho'_{xm1,2}) = 1/4\,(\,|\lambda_1| - |\lambda_2|\,)^2 \tag{45b}$$

$$P_x(\rho'_{xs1,2}) = 1/4\,(\,|\lambda_1| - |\lambda_2|\,)^2 \tag{45c}$$

$$P_c(\rho'_{xs1,2}) = 1/4\,(\,|\lambda_1| + |\lambda_2|\,)^2 \tag{45d}$$

The $P'_{cn1,2}$ of (49c) are co-pol nulls, because the power returned to the co-pol channel becomes zero, i.e.,

$$P_c(\rho'_{cn1,2}) = 0 \tag{46}$$

4.3 The Polarization Fork

In order to determine the "polarization fork operator of Huynen" [51], use is made of the complex polarization ratio ρ formulation [18], shown in Fig. 4.1, relating point (ρ′) on the complex plane with $P(\rho'_s)$ on the Poincaré) sphere [20,122].

$$\rho_{HV} = |\,\rho_{HV}\,|\,e^{j\,\delta_{HV}} = \left|\frac{E_V}{E_H}\right| e^{j\,(\delta_V - \delta_H)} = \tan\alpha_{HV}\,e^{j\,\delta_{HV}} =$$

$$= \frac{\tan\phi + j\tan\tau}{1 - j\tan\phi\,\tan\tau} \tag{47}$$

According to the complex polarization ratio formulation, each point ρ′ of the complex plane can be connected to the zenith (LC) of the sphere, resting tangent to the complex plane in its origin 0 at the nadir (RC), by a straight line that intersects the sphere at one point $P(\rho'_s)$ where the nadir (RC) corresponds to the origin (0) of the plane, the zenith (Z) to the circle at "infinity (∞)", and the equator to the unit circle, representing linear polarization states. Having established the one-to-one relationship between the Poincaré sphere and the complex plane, the polarization fork can easily be constructed as shown in Fig. 4.2.

According to definition (53) and Figs. 4.1a-c, the cross-pol NULL (co-pol Max) $\rho'_{xn1} = \rho'_{cm1} = 0$ is located at the origin of the complex plane, so the mapping point is X_1 (South pole: N) on the Poincaré sphere. And $\rho'_{xn2} = \rho'_{cm2} = \infty$ is the infinity of the complex plane, so the corresponding point is X_2 (North pole: Z). $X_1 X_2$ forms a diameter of the sphere and is perpendicular to the complex plane. Refer to Figs. 4.2a-c [123].

According to the expression of the cross-pol max and cross-pol saddles, they all lie on the unit circle and are the end points of two orthogonal diameters. So their corresponding points lie on the equator of the sphere as S_1, S_2, T_1, and T_2 with $S_1 S_2$ and $T_1 T_2$ perpendicular to each other. The co-pol nulls of $\rho'_{cn1,2}$ lie on the same straight line with $\rho'_{xm1,2}$ on the plane and symmetric about the origin 0, so their corresponding points on the sphere C_1 and C_2 lie on the same great circle with X_1, X_2, S_1, and S_2, symmetric about the diameter $X_1 X_2$. The complete Fork is shown in Fig. 4.2a and in alternate representations [19,122] are given in Figs. 4.2b-c.

4.4 Huynen's presentation [51]

In order to compare the results, illustrated in Fig 3.2b, for our scattering matrix [S] with that of Huynen's target matrix [T] of Fig. 3.2c, Huynen's geometric parameters (m, ϕ_m, τ_m, ν, γ, δ_m α_m) are introduced in Fig. 3.2c, where from (41) to (50), we find $4\nu = \phi_1 - \phi_2$, $\tan\gamma = (\,|\nu_2|/|\nu_1|\,)^{1/2}$, $\delta_m = arg\{\rho_1\}$, $\alpha_m = \tan^{-1}\{|\rho_1|\}$, $\phi_m = \frac{1}{2}\tan^{-1}\{\tan2\alpha_m \cos2\tau_m\}$, and $\tau_m = \frac{1}{2}\sin^{-1}\{\sin2\alpha_m \sin\delta_m\}$. Using Huynen's geometric parameters, the properties of the scattering matrix [S], as illustrated in Fig. 4.2a/b, can be expressed according to $[S'(AB)] = [U]^T [S] [U]$, as [118]

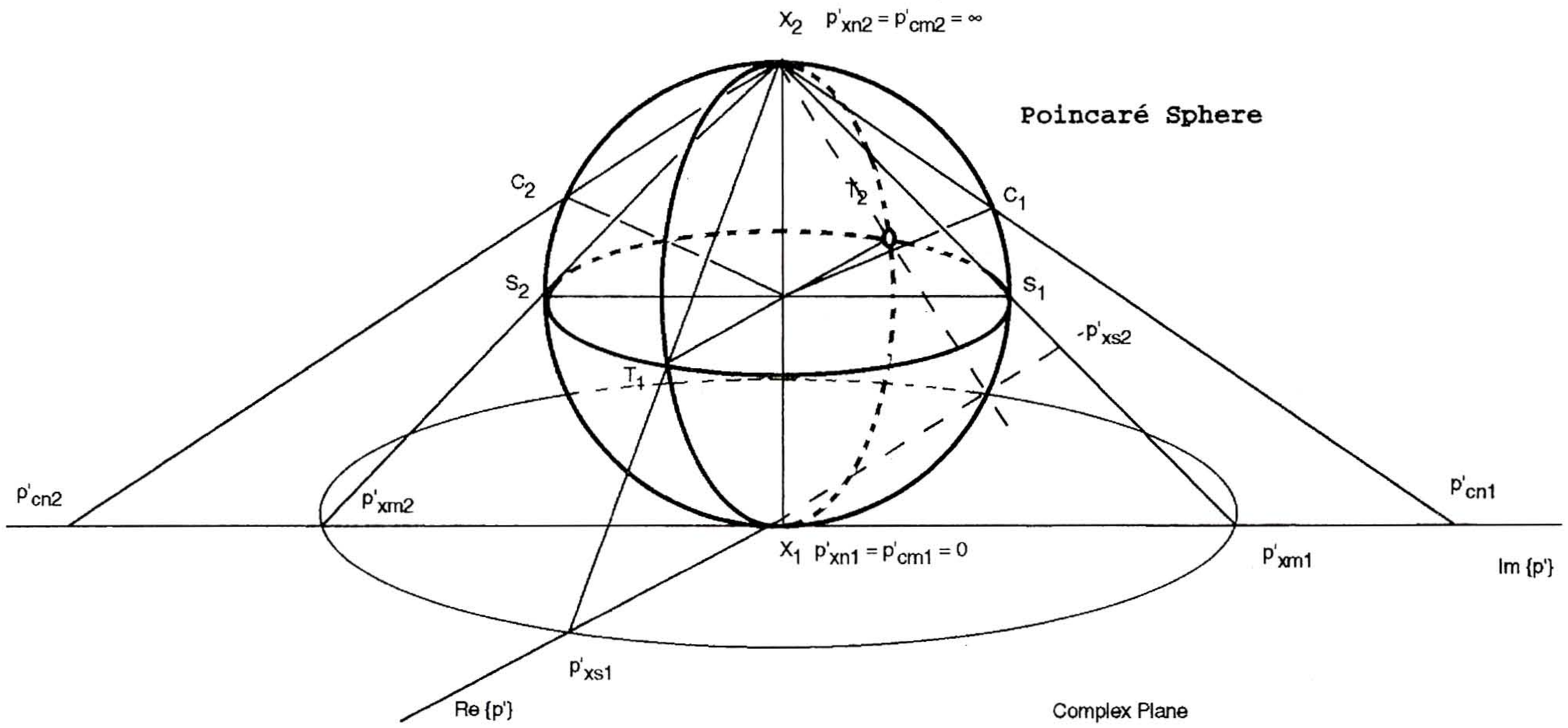

Fig. 4.2a - Correspondence of $\rho'_{xn1,2} = \rho'_{cm1,2}$, $\rho'_{xm1,2}$, $\rho'_{cn1,2}$ *on the complex plane with* $x_{1,2}$, $T_{1,2}$, $S_{1,2}$ *and* $C_{1,2}$ *on the Poincaré sphere.*

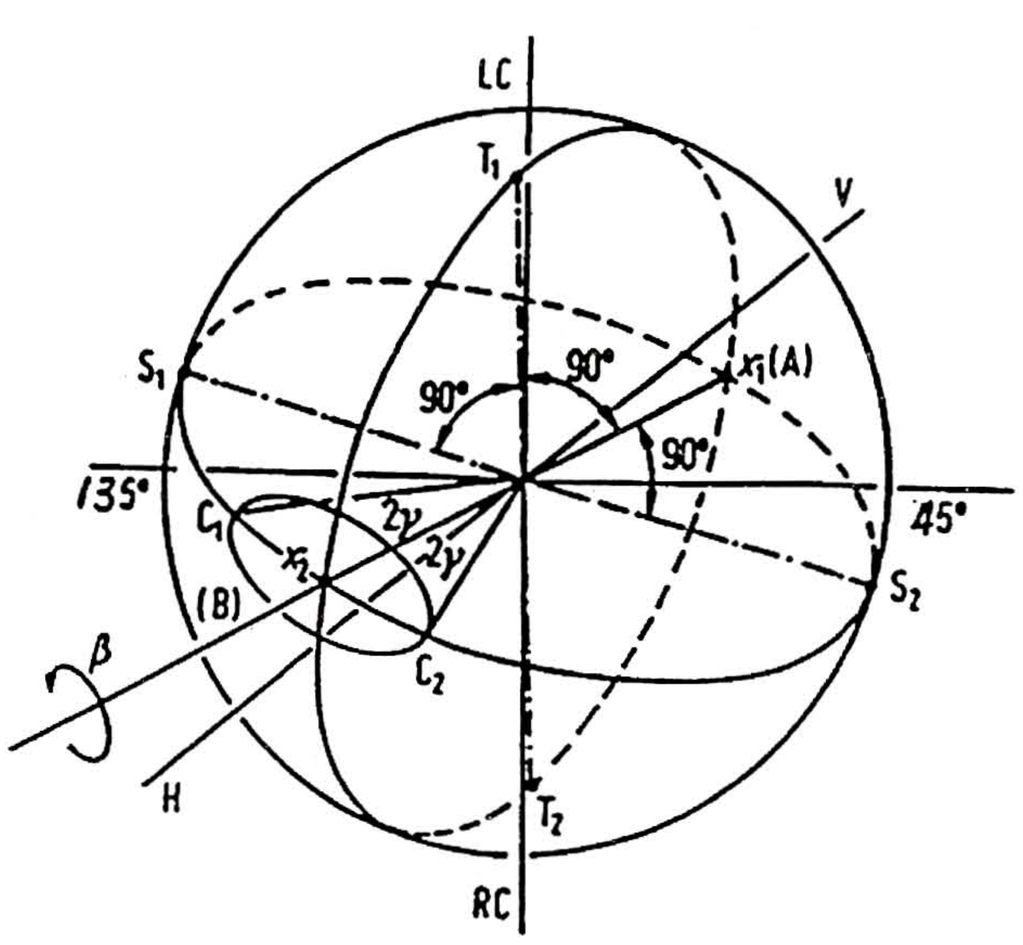

Fig. 4.2b - Representation of the characteristic polarization states on the Poincaré sphere (x_1*: cross-pol null and co-pol max;* x_2*: cross-pol null and co-pol extremum;* $c_{1,2}$*: co-pol nulls;* $s_{1,2}$*: cross-pol maxima;* $T_{1,2}$*: cross-pol saddle points;* γ*: target characteristic angle) presented in the new basis (AB).*

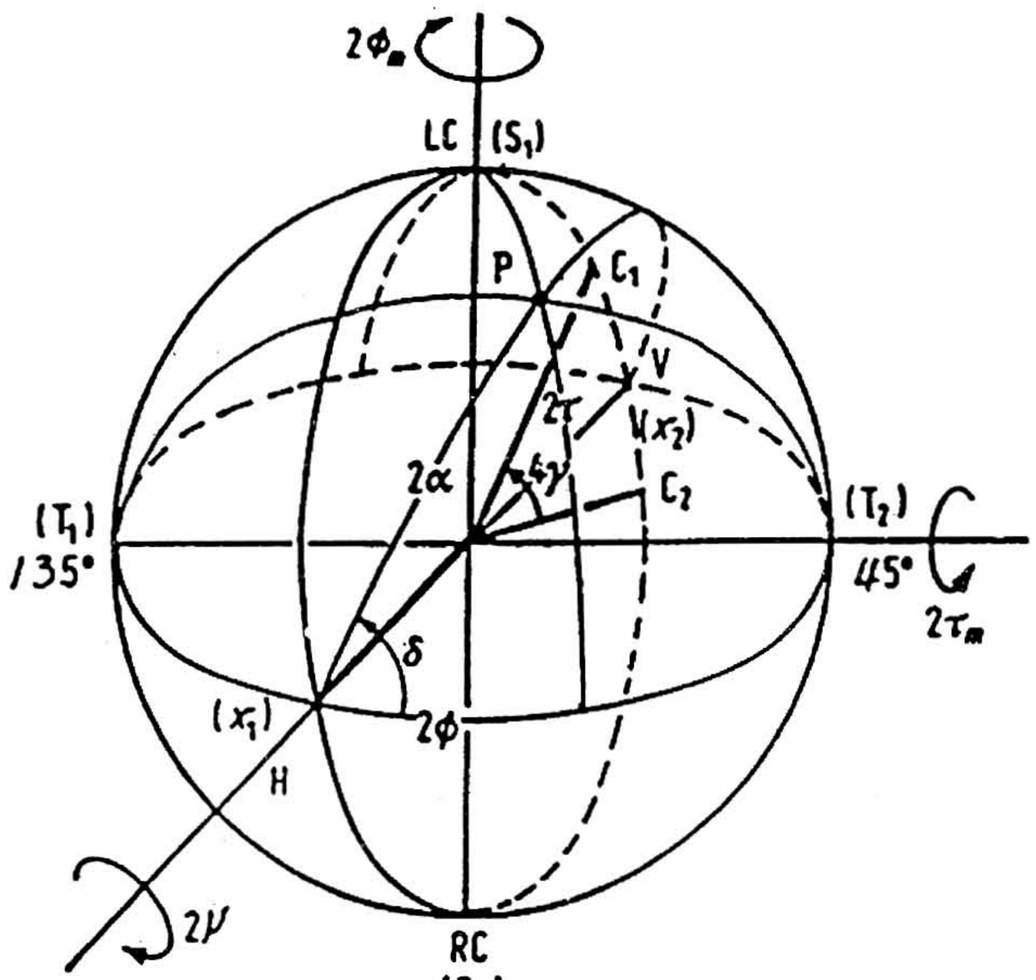

Fig. 4.2c - The standardized "Polarization Fork of Huynen" with definition of Huynen's geometric parameters presented in the "old basis".

m - traget size

ϕ - *target orientation or tilt angle*

ν - *target skip angle*

τ - *target ellipticity angle* (τ_m , δ_m *of co-pol max)*

γ- *target characteristic angle*

ρ - $\tan\alpha \exp j\delta$ - *polarization* (α_m , δ_m *of co-pol max).*

$$[S] = [U^*(\rho_1)] \exp(\nu [L]^*)\, m \begin{bmatrix} 1 & 0 \\ 0 & \tan^2\gamma \end{bmatrix} \exp(\nu [L]^*]^T [U^*(\rho_1)]^T \exp(j\xi), \quad (48a)$$

$$[U^*(\rho)] = \frac{1}{\sqrt{1+\rho_1\rho_1^*}} \begin{bmatrix} e^{-j\psi_1} & -\rho_1(\Phi_m, \tau_m)\, e^{-j\psi_4} \\ \rho_1^*(\Phi_{m'}\tau_m)\, e^{-j\Psi_1} & e^{-j\psi_4} \end{bmatrix} \quad (48b)$$

which is, as shown in [19] and illustrated in Fig. 4.2c, the same as Huynen's [H] given by

$$[H] = [U^*(\psi,\tau_m,\nu)]\, m \begin{bmatrix} 1 & 0 \\ 0 & \tan^2\gamma \end{bmatrix} [U^{*\prime}(\psi,\tau_m,\nu)] \exp(j\xi) \quad (49a)$$

and

$$[U(\psi, \tau_m, \nu)] = e^{\psi[J]}\, e^{\tau}\, m^{[K]}\, e^{\{}\nu [L], \quad (49b)$$

where j [J], j [K] and j [L] are the Pauli spin matrices [σ_i] and [I] is the identity matrix defined by:

$$[I] = \begin{bmatrix} 1 & 0 \\ 0 & 1 \end{bmatrix}; [J] = \begin{bmatrix} 0 & -1 \\ 1 & 0 \end{bmatrix}; [K] = \begin{bmatrix} 0 & j \\ j & 0 \end{bmatrix}; [L] = \begin{bmatrix} -j & 0 \\ 0 & j \end{bmatrix}$$

$$[K]^2 = [I]\ ;\ [L] = [J]\,[K] = -[K]\,[K = J]\ ;\ [L]^2 = [I]$$

with

$$e^{\psi[J]} = \begin{bmatrix} \cos\psi & -\sin\psi \\ \sin\psi & \cos\psi \end{bmatrix}, e^{\tau_m[K]} = \begin{bmatrix} \sin\tau & j\sin\tau \\ j\sin\tau & \cos\tau \end{bmatrix}, e^{\nu[L]} = \begin{bmatrix} e^{-j\nu} & 0 \\ 0 & e^{j\nu} \end{bmatrix}$$

4.5 The complete polarimetric matched image filter

The complete PMIF utilizes the properties of the 'Polarization Fork' concept on a pixel-by-pixel basis [113], and fully integrates the concept of the localized characteristic polarization state approach into the optimization solution. Currently, this approach is being further generalized by including direct optimization procedures for the Mueller (Kennaugh) power matrix. These very extensive generalizations of the hitherto limited PMIF approach are beyond the scope of this paper and will be the subject of future publications.

5. STATISTICAL ANALYSIS IN DIGITAL IMAGE PROCESSING

To classify various terrain types of coherent SAR images, efficient interpretations must be used to reduce the amount of CPU time required. Here, an approach of classification via the scattered wave amplitude and phase statistics [33,61] is introduced which provides some information about terrain surface roughness. The simplest random uncorrelated rough surface model produces Rayleigh amplitude statistics while the presence of correlations is likely to result in deviations from Rayleigh behavior such as Rice, Weibull, etc. Rough surface scattering and the related speckle phenomenon as seen in POL-SAR (Fig. 5.1) has long been known in highly coherent laser applications as will be shown in the following sections.

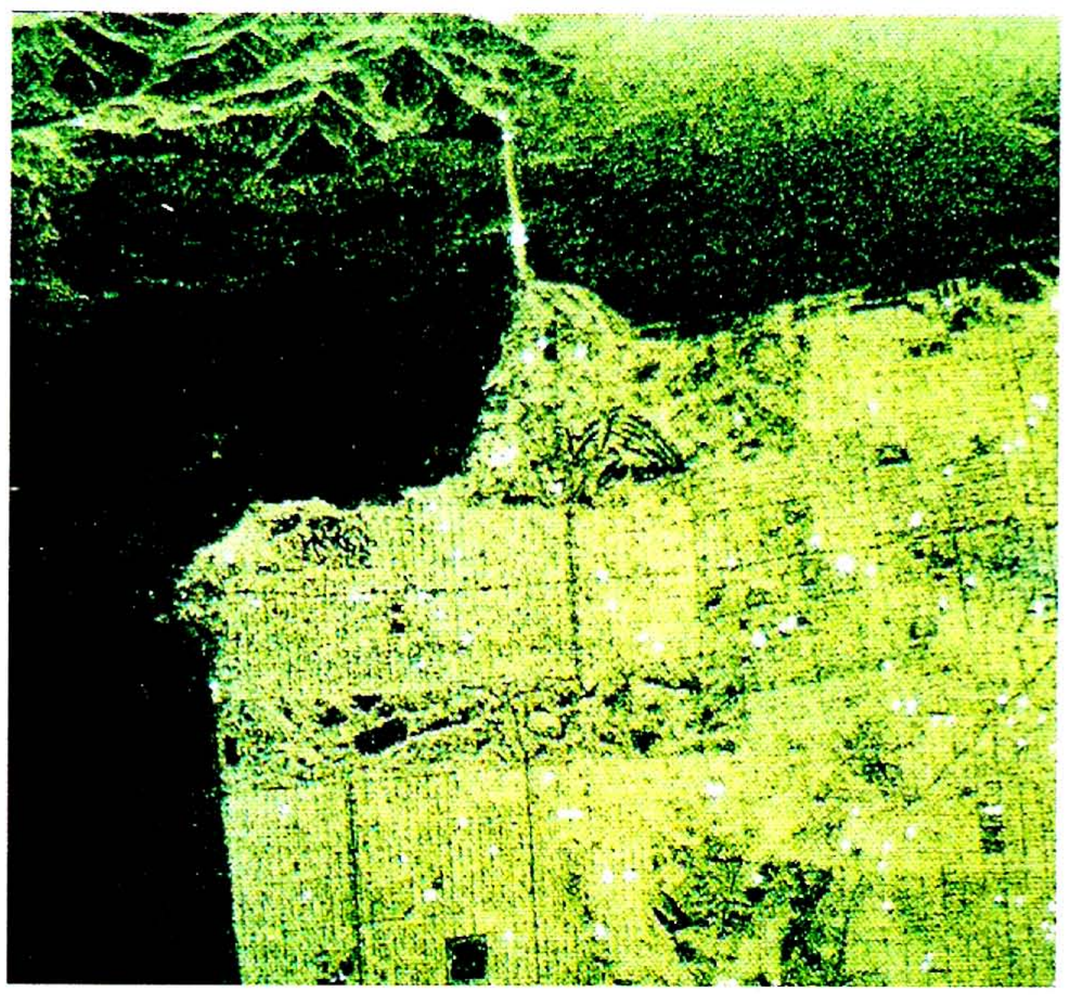

Fig. 5.1 - POL-SAR image of NASA/JPL CV-990 San Francisco Bay - Golden Gate Bridge Site.

5.1 Random Walk of Phasors in Coherent Imaging

The occurrence of speckle is a well-known obstacle in the interpretation of coherent imaging. Highly coherent laser light, for instance, produces granular images which do not seem to represent the macroscopic properties of an illuminated object. A surface is rough on the scale of an incident wavelength and the result of scattering off such a surface is a wave which is randomly modulated in phase (Fig. 5.2). The result is a granular intensity pattern known as speckle. When dealing with large data sets containing speckle, it is quite useful to conduct a statistical evaluation with two goals in mind: identifying and removing speckle and noise

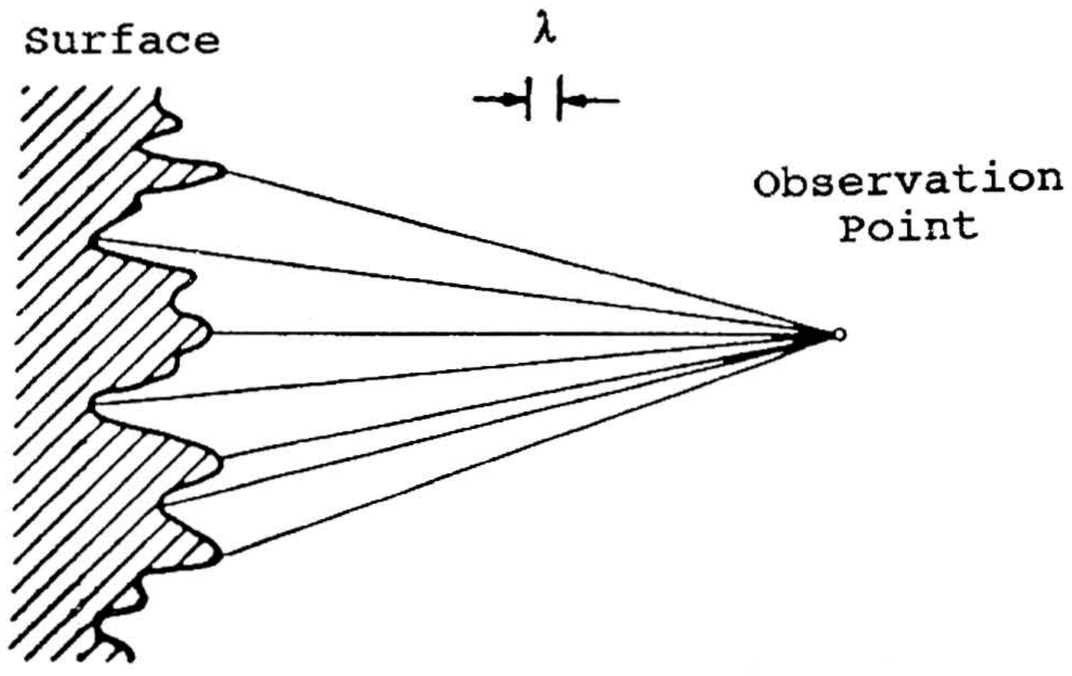

Fig. 5.2 - Rough Surface Scattering [28].

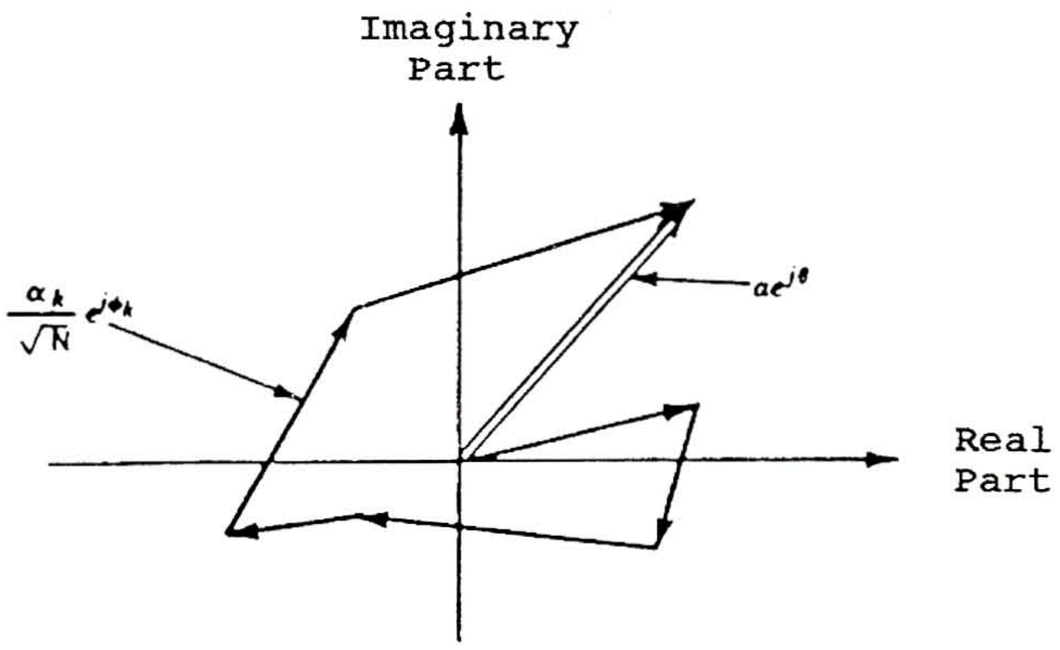

Fig. 5.3 - Random Walk of Phasors [46].

and determining surface structure based on roughness criteria.

Suppose, the phasor A is the sum ("random walk in the complex plane") of many elementary phasor contributions, representing the amplitude and phase of a monochromatic wave disturbance (Fig. 5.3).

$$\vec{A} = ae^{j\theta} = \frac{1}{\sqrt{N}} \sum_{k=1}^{N} \alpha_k \, e^{j\theta_k} \tag{50}$$

If all the amplitudes and phases of every elementary phasor are statistically independent of each other, then the phases are distributed uniformly between $(-\pi, +\pi)$ which is an indication for a rough surface at this wavelength. The expressions for intensity and phase are:

$$E = \sqrt{u^2 + v^2}\,, \quad \theta = \tan^{-1}\left(\frac{v}{u}\right) \tag{51}$$

where $E \geq 0$, $0 \leq \theta \leq 2\pi$, , and u, v are general intensity and phase term components.

The resulting univariate probability density function (PDF) for the real part is:

$$P(u) = \frac{1}{2\pi^2} \exp\left(\frac{-u^2}{2\sigma^2}\right) \tag{52}$$

where the mean is assumed to be zero and,

$$\sigma^2 = \lim_{N \to \infty} 1/N \sum_{k=1}^{N} < | a_k |^2 > ,$$

also known as the variance.

In the PDF of the imaginary part, the variable u is replaced by v. Similarly, the joint PDF of the univariate densities results in the joint, circular Gaussian density function:

$$P(u,v) = \frac{1}{2\pi\sigma^2} \exp\left(-\frac{u^2 + v^2}{2\sigma^2}\right) \tag{53}$$

In polar coordinates (magnitude and phase statistics), u=a cosθ and v=a sinθ such that

$$P(a\,,\theta) = \begin{cases} \dfrac{a}{2\pi\sigma^2} \exp\dfrac{-a^2}{2\sigma^2} & -\pi < \theta \leq \pi \\ & a > 0 \\ 0 & otherwise \end{cases} \tag{54}$$

The univariate density P(a) is found by integrating P(a,θ) with respect to θ, such that

$$P(a) = \int_{-\pi}^{\pi} P(a,\theta)\, d\theta = \begin{cases} \dfrac{a}{\sigma^2} \exp\left(-\dfrac{a^2}{2\sigma^2}\right) & a > 0 \\ 0 & otherwise \end{cases} \tag{55}$$

which is the so-called Rayleigh density function, having mean and variance of

$$\vec{a} = \sqrt{(\pi/2)\,\sigma}\,; \quad \sigma_2 = [2 - \pi/2]\,\sigma^2\,.$$

Similarly, the univariate density P(θ) is given as

$$P(\theta) = \begin{cases} \dfrac{1}{2}\displaystyle\int_{\pi}^{\infty} \frac{a}{\sigma^2} \exp\left(-\frac{a^2}{2\sigma^2}\right) da & -\pi < \theta \leq 0 \\ 0 & otherwise \end{cases} \tag{56}$$

Note, that the integral corresponds to the integral of the Rayleigh density function being unity, hence

$$P(\theta) = \begin{cases} \dfrac{1}{2\pi} & -\pi < \theta \leq \pi \\ 0 & otherwise \end{cases} \tag{57}$$

Suppose, the Gaussian sampling functions have shifted means and different variances which is equivalent to adding constant vectors to the resultant phasors from the "walk in the complex plane" so that

$$\vec{A} = S + \frac{1}{\sqrt{N}} \sum_{k=1}^{N} (a_k \cos\theta_k + a_k \sin\theta_k) , \tag{58}$$

then the joint PDF is simply expanded to the general form

$$P(u,v) = \frac{1}{2\pi\sigma_u\sigma_v} \exp\left(\frac{-[u-s_u]^2}{2\sigma_u^2} \; \frac{-[v-s_v]^2}{2\sigma_v^2} \right) \tag{59}$$

In terms of magnitude and phase statistics, the joint PDF becomes

$$P(a,\theta) = \begin{cases} \dfrac{a}{2\pi\sigma_u\sigma_v} \exp\left(\dfrac{-[a\cos\theta - s_u]^2}{2\sigma_u^2} \; \dfrac{-[a\sin\theta - s_v]^2}{2\sigma_v^2} \right) & \begin{matrix} a > 0 \\ -\pi < \theta \\ \theta \le \pi \end{matrix} \\ 0 & \textit{otherwise} \end{cases} \tag{60}$$

The univariate density function in polar form is

$$P(a) = \int_{-\pi}^{\pi} p(a,\theta)\, d\theta \tag{61}$$

$$= \frac{a}{2\pi\sigma^2} \exp\left(-\frac{a^2+s^2}{2} \right) \int_{-\pi}^{\pi} \exp\left(\frac{as}{\sigma^2} \cos\theta \right) d\theta$$

The integral may be expressed as $2\pi I_0 (as/\sigma^2)$, where I_0 is a modified Bessel function of the first kind and zero order which results in a Ricean density function [46,121]:

$$P(a) = \begin{cases} \dfrac{a}{\sigma^2} \exp\left(-\dfrac{a^2+s^2}{2\sigma^2} \right) I_0 \dfrac{as}{\sigma^2} & a > 0 \\ 0 & \textit{otherwise} \end{cases} \tag{62}$$

The following figures show several magnitude PDFs of a Ricean distribution where the shape of the PDF changes from a Rayleigh density to a Gaussian shifted by s as s increases (Fig. 5.4 & 5.5).

The corresponding phase PDFs are shown next, where the distribution changes from a straight line for a Rayleigh density to a bell-shaped curve as the phasor constant increases.

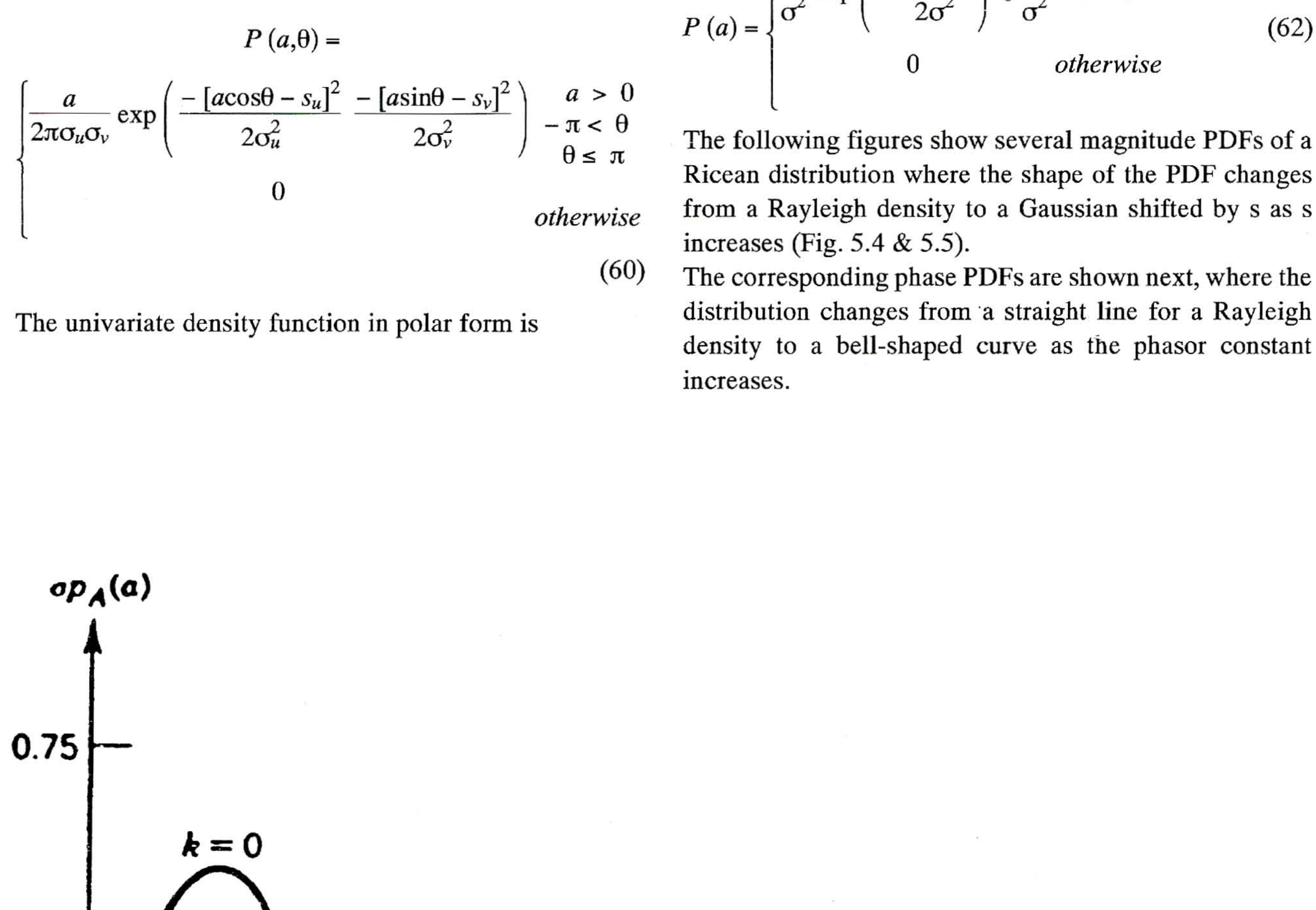

Fig. 5.4 - PDF of amplitude A of the sum of a constant phasor (length s) and a random phasor sum; $k = s/\sigma$ [46].

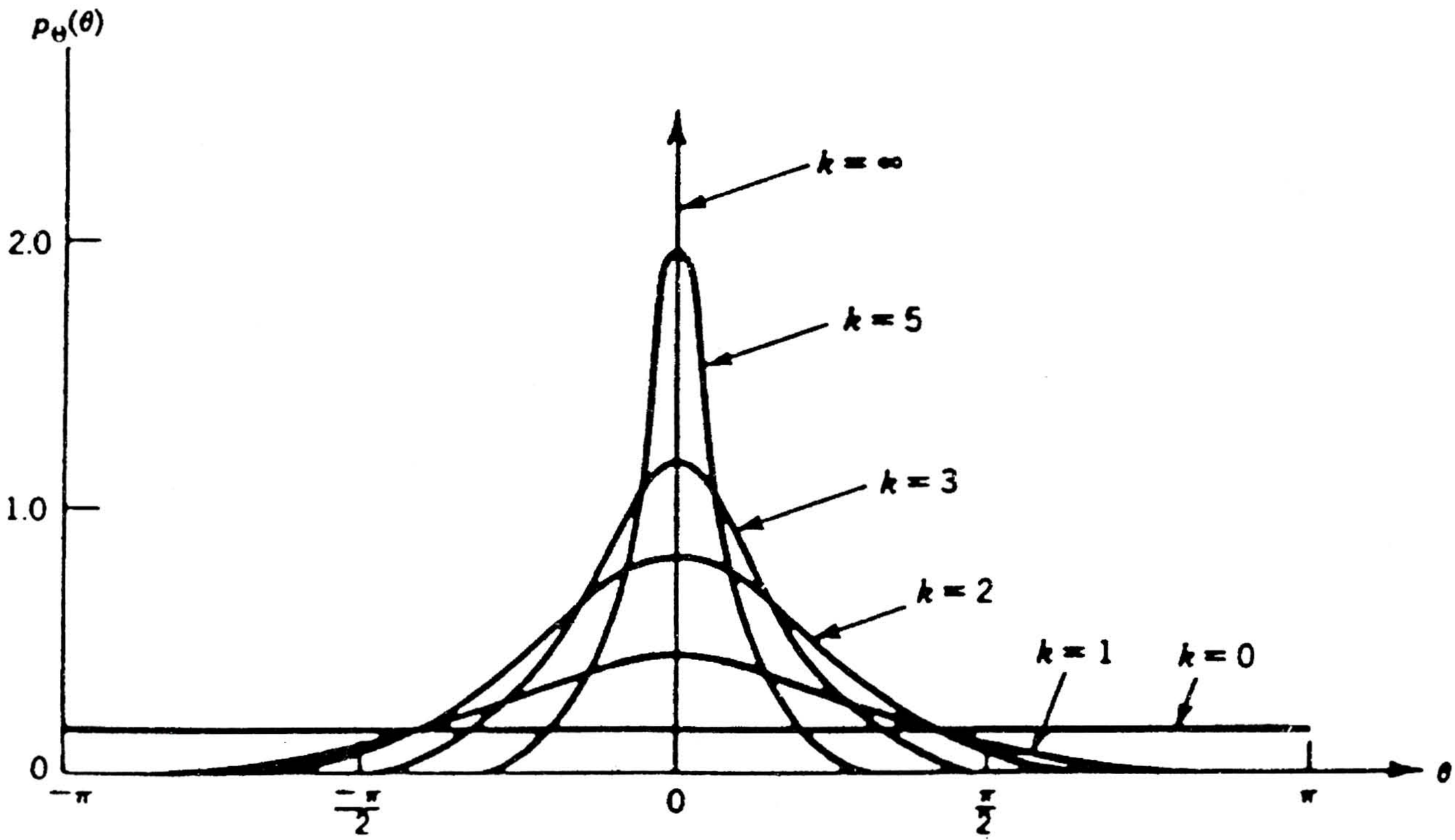

Fig. 5.5 - PDF for the phase for a constant phasor and a random phasor sum; $k = s/\sigma$ [46].

5.2 Statistical Analysis and Interpretation of the CV 990 SAR Image Parameters

In this section, it will be shown that an investigation of the basic complex POL-SAR data reveals a great deal about the type of scatterer in terms of its roughness. At microwave frequencies, the earth's surface is assumed to be a surface with different roughness regions, no matter whether the scattered region is ocean, vegetation or rock. This assumption reduces the statistical process simply to a determination of how much the distribution deviates from Rayleigh behavior. Three structurally uniform regions were chosen from a horizontal band located halfway between the top and the bottom of the image as shown in figure 5.6.

5.2.1 PDFs of Magnitude and Phase POL-SAR Components

The magnitude PDF of ocean returns are expected to resemble Rayleigh statistics [39,81,88,91,94,96, 102,103,111] more closely than the returns of the city region, since the ocean surface has fewer structured components in the image except for bridges, ships, breakwaters, and other man-made structures. Furthermore, since the ocean surface is relatively smooth, it acts like a flat plate reflecting EM radiation away from the obliquely oriented receiver. The city region, however, consists of many corner reflectors which reflect back much of the energy, which shows up as recognizable terrain features in the image.

The magnitude PDFs of the three selected regions: ocean, city and park, as shown in Figure 5.6 look Rayleigh distributed, while the associated phase PDFs are all uniformly distributed. The means and variances of the magnitudes of the individual image regions tend to agree with the fact that less speckled radar returns shift the PDF towards a Gaussian curve [41] as seen for the ocean, while more speckled image regions have skewness and kurtosis deviations from the Gaussian as well as shifted means.

These simple PDFs show a trend of the image data being generally Rayleigh distributed. It is, however, not possible from these PDFs to differentiate clearly between different terrain types, hence our statistical evaluation needs to be taken a step further [9,60,94,96,111,118-120].

Another approach is to make use of the circular Gaussian theorem [27,45] which states that if the means and stand-

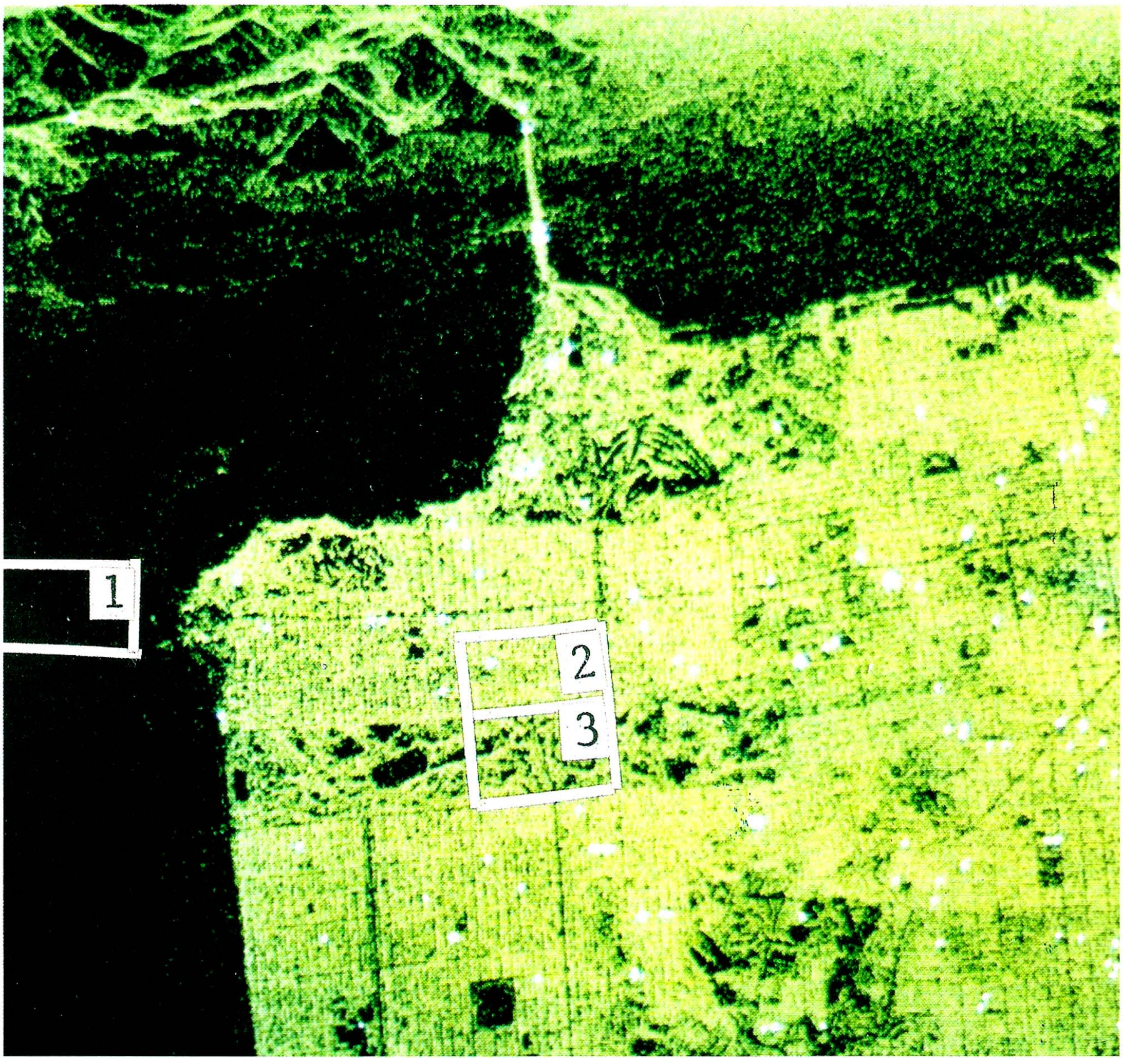

Fig. 5.6 - Image depicting the selected image region for ocean (1), city (2), and park (3).

ard deviations of the real and imaginary data components are identical, the distribution will be truly Rayleigh, i.e. the events are totally random and unstructured. Conversely, if the means and variances differ, then the image has structure which is different for various surface roughnesses [85].

5.2.2 PDFs of Real and Imaginary Components

The PDFs of the real and imaginary parts of the selected image regions are shown in Figs. 5.4, 5.5. All distributions are Gaussian and while the respective means and variances of the ocean and park regions are sufficiently similar, the city region exhibits a shifted mean of the imaginary distribution to the right. As discussed in the previous section, the shift of the mean of the imaginary distribution implies that a constant vector is added to every phasor

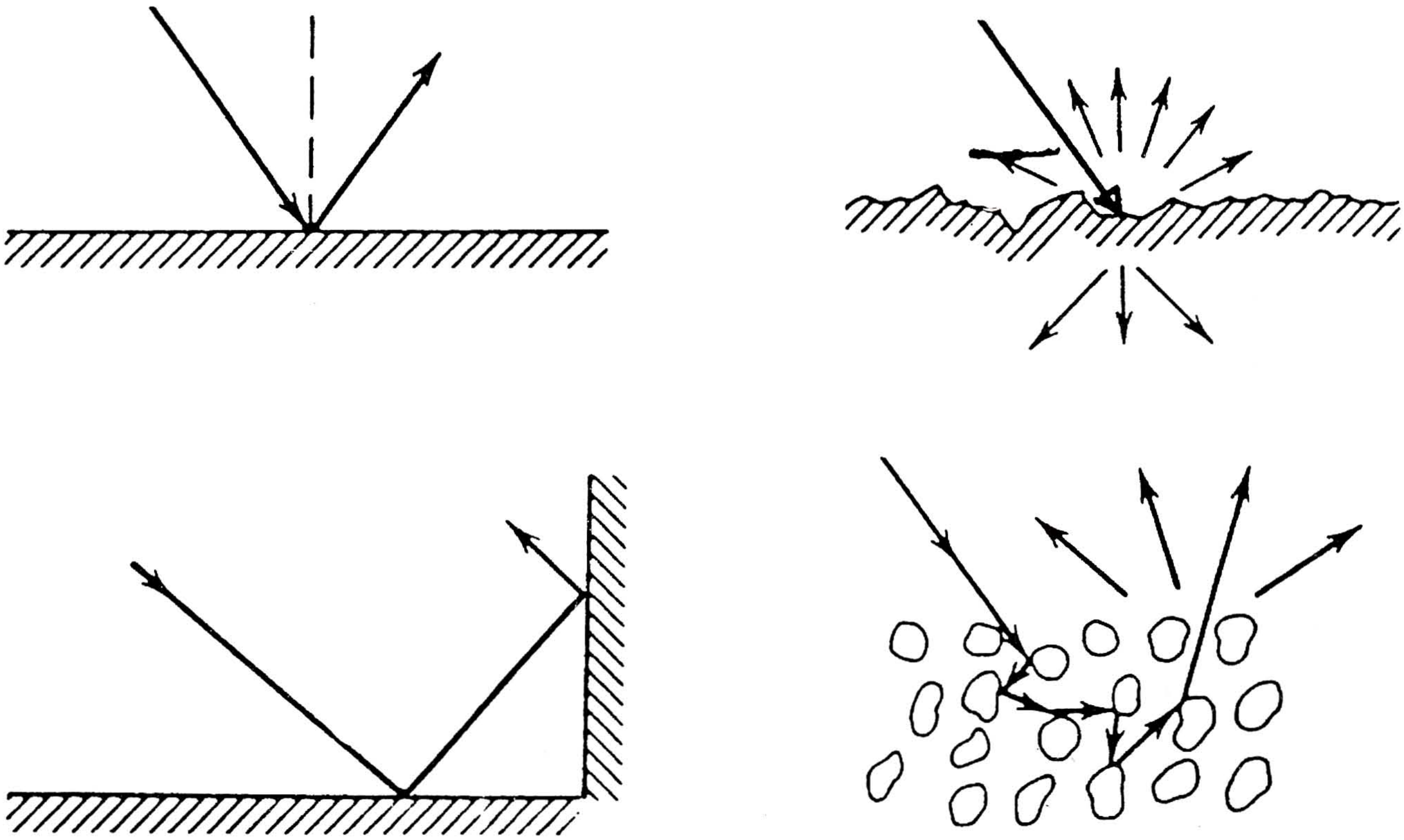

Fig. 5.7 - Pictorial description of the scattering process of some basic terrain.

resulting from a walk in the complex plane which is an indication that the density function is not Rayleigh but Ricean distributed. A guess at what might contribute a constant phasor is that the angular geometry of the city contains many strongly reflecting corner reflectors.

5.2.3 PDFs of Phase Differences of the POL-SAR Components

It can be assumed that the POL-SAR data set contains a great deal of noise and speckle which should be eliminated to get a clearer image of the underlying structure within the selected image regions. It would be ideal if the noise components cancel out of the following ratio:

$$\frac{S_{HH}\,(noisy)}{S_{VV}\,(noisy)} \Rightarrow \frac{S_{HH}}{S_{VV}}\,(noice\text{–}reduced) \tag{63}$$

The choice of the co-polarized components seems best if the channels for H and V have good separation. It turns out that the ratio of the magnitudes (Mag_{HH}/Mag_{VV} looks Rayleigh distributed and does not differ much from the magnitude PDFs of either one of the components. The phase differences ($\theta_{HH} - \theta_{VV}$), however, contain a surprising amount of image information as shown in Fig. 5.10.

Note, that the phase difference PDFs of the three regions consist of the phase differences between the same pixels of the appropriate data sets (e.g. HH(10,18) < -- > VV(10,18), etc.), before generating the distribution.
The basically very unique PDFs between the three image regions may be called target/terrain signatures based on their surface roughness. Furthermore, the shifted peak of the city region might be attributed to a π-phase shift due to the presence numerous corner reflectors.

5.3 Application to CV 990 and Discussion of Results

The results indicate that a statistical evaluation of the polarimetric SAR data set is very useful, especially in getting a "feeling" for the amount of structure versus unstructured noise and speckle components. It seems that speckle statistics can be used by itself to classify terrain in terms of surface roughness. A relatively smooth surface

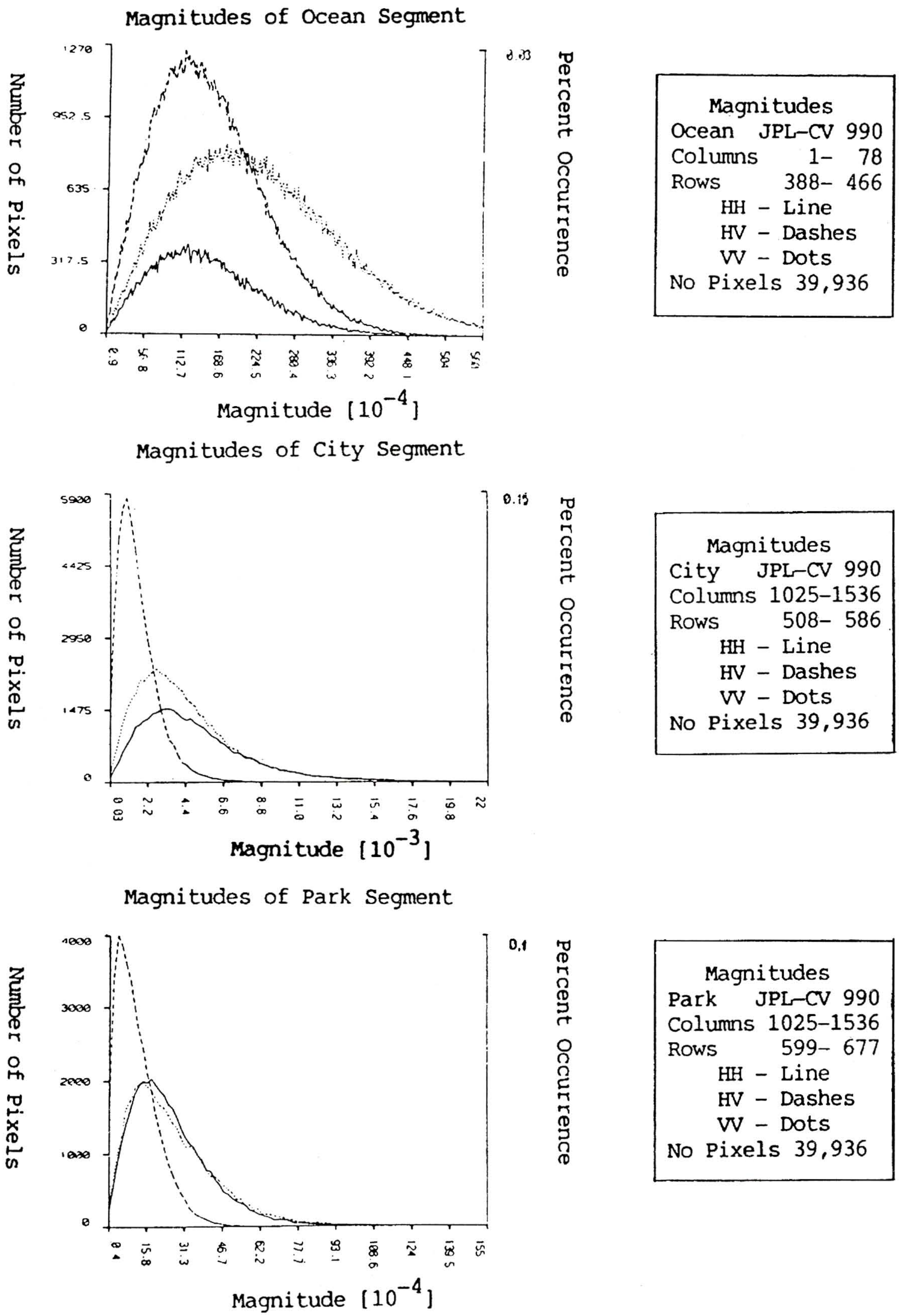

Fig. 5.8 - Magnitude PDFs of Ocean, City, and Park Regions.

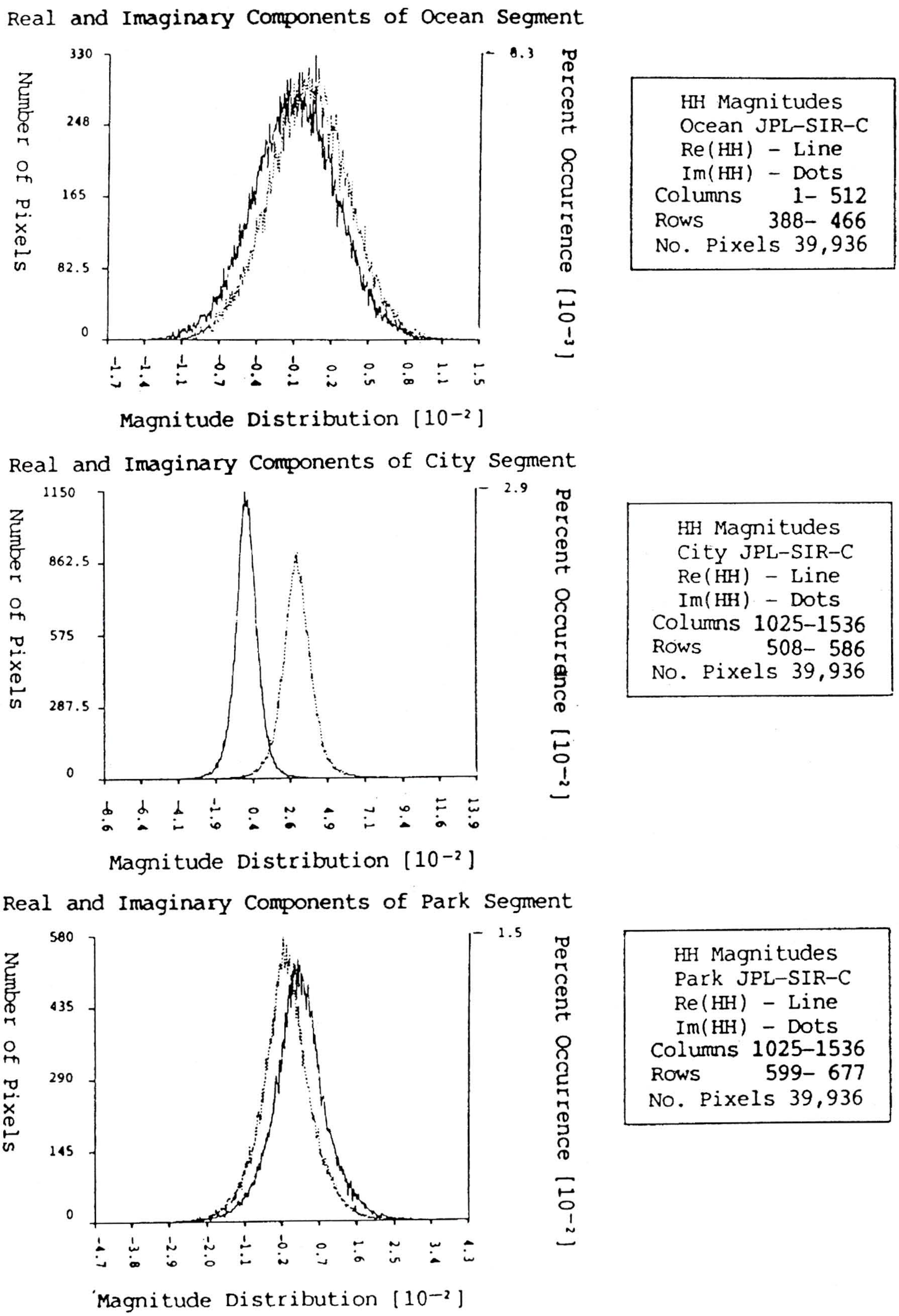

Fig. 5.9 - PDFs of real and imaginary components of Ocean, City, and Park Regions.

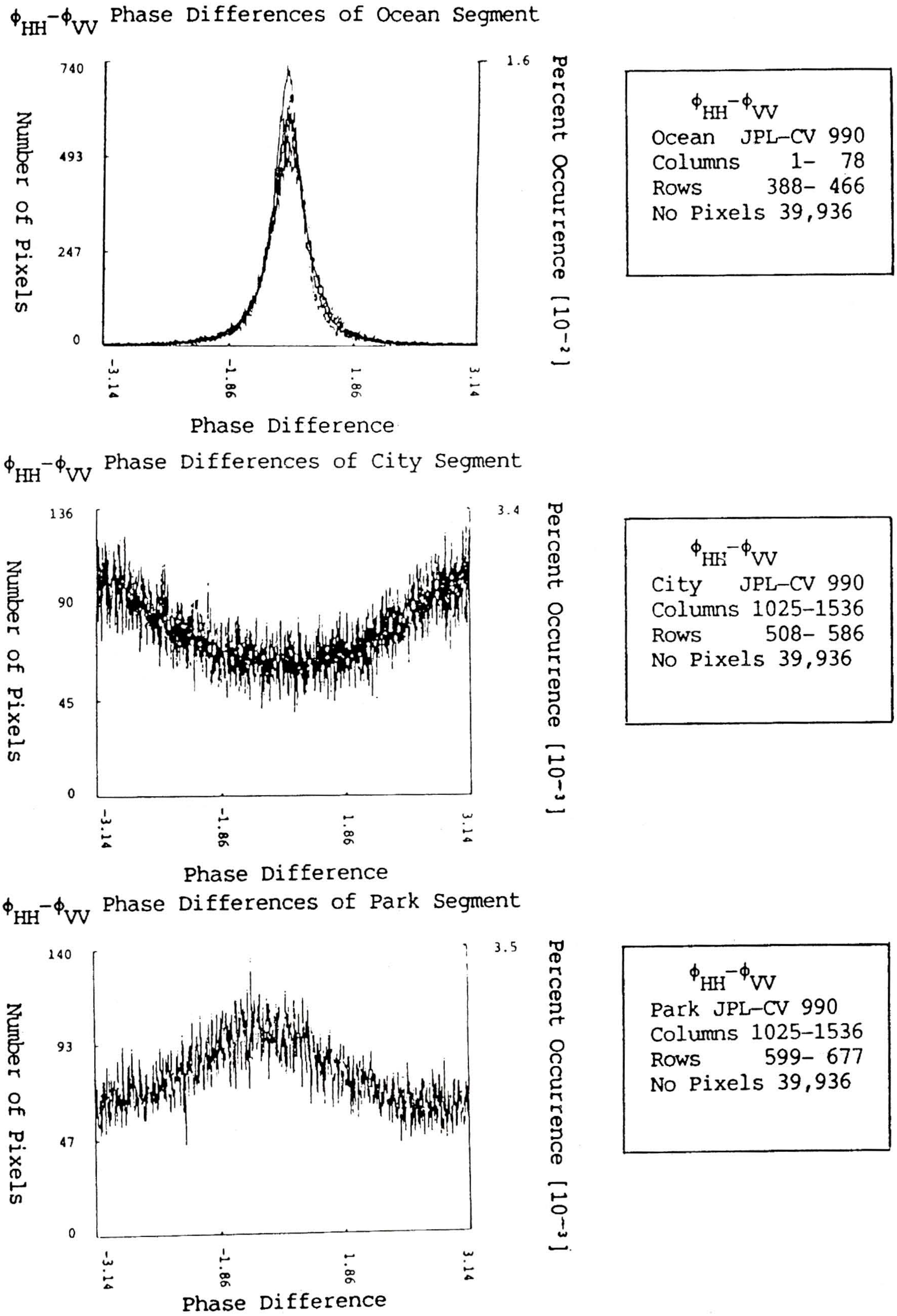

Fig. 5.10 - PDFs of phase differences of Ocean, City, and Park Regions.

like ocean has a very narrow variance while the corner reflectors of the city and, to some extent, vegetated areas, spread the distribution. It is necessary, however, to compare at least two distributions of, say, ocean versus city to clearly see the difference. Whether the "structured speckle distribution" of the city region really contains a constant phasor is not confirmed and could be coincidental or perhaps a calibration problem.

These preliminary results, particularly the shifted means of the city segment in terms of real and imaginary components, are promising but one should be cautious. This is the first time a POL-SAR data was investigated statistically and documented in this fashion. Furthermore, the radar equipment does not exist anymore, making it impossible to obtain more and better data sets. It also seems that the equipment was not very well calibrated at times hence the phase information cannot be trusted. Nevertheless, the statistics is promising and should be tested on new POL-SAR data sets.

5.3.1 Speckle Displacement Along the Path of Flight Due to Motional Ground Scatter

Two other phenomena on the image (see Figure 5.1) consist of the dotted lines parallel to the Golden Gate Bridge as well as the shaded regions near the ocean/city boundary along the coast line on the left side of the image. Sometimes, speckle is displaced orthogonally to the swath by more than a speckle diameter, apparently due to movement within the resolution cell of the speckle. Another possibility might be the presence of two strong and similar scatterers inside one pixel resolution cell or neighboring pixels. In either sace, strong scatterers may actually have strong diffraction patterns which interfere constructively at certain displacements from these bright pixels in the image (refer to Young's fringe patterns in optics [28].

5.3.2 Displacement Due to Diffraction or Multiple Scattering

Suppose, the angular distribution of the fringes is

$$d_i \sin\beta = n\lambda \tag{64}$$

where n is the nth order interference maximum in the direction d_i, then the vector displacement d_0 of the object would be given as

$$d_0 \frac{d_i}{M} = \frac{n\lambda}{M \sin\beta} \tag{65}$$

where M corresponds to a magnification factor, possibly related to the dielectric properties of the scatterer with respect to its surroundings (e.g., metallic surface or tall beam vs. rocky and vegetated terrain or water). The speckle translation due to the diffraction interference phenomenon described above, although speculative, may explain the bright pixels connected to lines as seen on either side of the Golden Gate Bridge. This bridge is supported by two tall twin towers which are located near the bright horizontal lines connecting the brightest displaced pixels near the ends of the bridge. Two very thick parallel suspension cables span between the towers in an arc from which more vertical cables reach down to the sides of the roadway.

5.3.3 Displacement Due to Motional Ground Scatter Doppler Shifts

The other likely possibility of motion within a resolution cell, by a moving car, for instance, seems feasible that this motion has an effect (Doppler shift) on neighboring image cells.

The "ghost image" of the city along the left coast line may also be described by displacement due to diffraction or to motional Doppler shifts. The numerous adjacent strong scatterers (corner reflectors) of the city are displaced into the ocean region where they are contrasted well against the dark ocean which does not scatter back much energy towards the antenna. The park region of the image does not produce a "ghost image" as strongly as that of the city which might be interpreted as the presence of fewer corner reflectors or flat surfaces, i.e. man-made structures, including moving vehicles. It is assumed that a similar "ghost image" is projected in the opposite direction, i.e. to the right but not visible because of the brighter city image. Another possibility of obtaining a coherent superposition of diffraction effects is to rotate or vibrate either the terrain surface or, of course, the radar platform mounted to the aircraft. The latter is quite likely, considering that the image was taken over a 10 km stretch during eight minutes of flight. Hence, many of the displaced pixels may be attributed to minute fluctuations of the flight path.

Yet another method of speckle (pixel) displacement involves Fourier transformation during post-processing procedures of the image which was done before this image data set was made available to this author. If the nearest sidelobes of every pixel in the frequency domain are very high, due to the effects of constructive diffraction interference, the result in the time domain may be the pixel itself as well as two adjacent but less intense pixels translated to either side which is a phenomenon observed in microwave astronomy [28].

CONCLUSION

In this monograph, a concise overview was presented on how complete polarization information in POL-SAR image analysis may be utilized to further improve our various existing standard methods of speckle reduction. Specific emphasis was placed on developing the concept of the "Limited Polarization Matched Image Filter" at first, and extending it to include the complete set of characteristic polarization states into its formulation which requires extensive further advancement so that this method can be applied successfully to the optimization of image discriminants in POL-SAR image analysis [117].

ACKNOWLEDGEMENTS

This research was supported, in part, by the U.S. Office of Naval Research, Arlington, VA, under contract US ONR N00014-C-0773; by the U.S. Naval Air Systems Command, Washington, DC, under contract US ONR N00019-81-C-0352; by the U.S. Naval Air Development Center, Warminster, PA, under contracts USONR N00019-82-C-0306 and N62269-85-C-0383; by the Army Research Office, Res. Tri. Park, NC, under contracts DAA629-80-K0027 and DAAK-84-C-0101; by the U.S. Army MICOM, Advanced Sensors Laboratory, Redstone Arsenal, AL, under contract DAA023-86-D-0001; by the NATO Scientific Affairs Division, Grants SA.5-2IMOR.2038-(189)84 and SA.5-2-05RA0653(85); and by the Johns Hopkins University, Applied Physics Laboratory, under Purchase Order No. 513542-0. We wish to express our sincere gratitude to our contract scientists, Drs. James W. Mink, Walter A. Flood and Karl H. Steinbach of the U.S. Army (ARO, BRDEC); Lloyd W. Root and Brenda L. Matkin of the U.S. Army Missile Laboratory; Drs. Henry W. Mullaney, Richard G. Brandt, James G. Smith and Arthur K. Jordan (ONR), Otto Kessler (NADC), Donald R. Wehner (NOSC), Dean A. Mensa (PMTC), Robert J. Dinger (NWC) of the U.S. Navy; and especially Dr. John Apel of the Johns Hopkins University, Applied Physics Laboratory for their suggestions and continued support of the research.

REFERENCES

[1] Agrawal, A.P. & Boerner, W.-M. (Jan. 1989) "Re-Development of Kennaugh's Characteristic Polarization Theory Using the Polarization Ratio Formalism for the Coherent Case", IEEE Trans. on Geoscience Electronics, Vol 27, No. 1, pp. 2-14.

[2] Amin, A.T. (1977) 'An Algorithm for Gray-Level Transformations in Digital Images', IEEE Trans. on Computers, 26, pp. 1158-1161.

[3] Barnes, R.M. (June 1984) Detection of a Randomly Polarized Target, Ph.D. Thesis, Department of Electrical Engineering, Northeastern University, Boston, Massachusetts.

[4] Barakat, R. (Jan. 1981) 'Direct Derivation of Intensity and Phase Statistics of Speckle Produced by a Weak Scatterer from the Random Sinusoid Model', J. Opt. Soc. Am., Vol. 71, No. 1.

[5] Barakat, R. (Jan 1981) 'First-Order Statistics of Combined Random Sinusoidal Waves with Applications to Laser Speckle Patterns', J. Opt. Soc. Am., Vol. 71, No. 1.

[6] Barakat, R.: (1986) 'Weak-scatter generalization of the K-density function with application to laser scattering in atmospheric turbulence', JOSA A,3 3, pp. 401-409 (1986).

[7] Beckman, P. & Spizzichino, A. (1963) The Scattering of EM Waves from Rough Surfaces, MacMillan, N.Y.

[8] Bernstein, R. (1978) Digital Image Processing for Remote Sensing IEEE Press, J. Wiley Publ., N.Y.

[9] Bevington, P.R. (1969) Data Reduction and Error Analysis for the Physical Sciences, McGraw-Hill, N.Y.

[10] Blom, R.G. et al. (July 1982) 'Radar Image Processing for Rock-Type Discrimination', IEEE, Vol. GE-20, No. 3, pp. 343-351.

[11] Boerner, W-M., Gniss, H, Magura, K. & al. (1978) Polarization dependence of image fidelity in microwave holographic mapping systems, 1978, AP-S Symp. Washington, DC, 1978, May 15-19, Proc. pp. 38-41.

[12] Boerner, W-M. (Sept. 1980) Polarization Utilization in Electromagnetic Inverse Scattering, Chapter 7 in Inverse Scattering Problems in Optics, Vol. II (ed. H.P. Baltes), *Topics in Current Physics*, Vol. 20, pp. 237-305, Springer Verlag.

[13] Boerner, W-M. (1980) Polarization Microwave Holography: An Extension of Scalar to Vector Holography (invited), 1980 International Optics Computing Conference, SPIE's Techn. Symposium East, Washington, DC, 1980-04009, (S-3B, 231-23) Proc. pp. 188-198.

[14] Boerner, W-M. (Nov/Dec 1981) "Use of Polarization in Electromagnetic Inverse Scattering", Radio Science, Vol. 16(6) (Special Issue including papers: 1980 Munich Symp. on EM Waves), pp. 1037-1045.

[15] Boerner, W-M. et al. (eds.) (Jan. 1985) Proceedings of the NATO-Advanced Research Workshop on *Inverse Methods in Electromagnetic Imaging* (18-24 Sept. 1983, Bad Windsheim, FR-Germany), Parts 1&2. NATO-ASI Series C-143 (1500 pgs.), D. Reidel Publ. Co.

[16] Boerner, W-M., Foo B.-Y., Eom, H.J. (Jan. 1987) "Interpretation of the Polarimetric C-Polarization Phase Term ($\phi_{HH} - \phi_{SS}$ in High Resolution SAR Imaging Using the JPL CV-990 Polarimetric L-Band SAR Data", Special IGARSS'85 Issue of the IEEE Transactions on Geoscience & Remote Sensing, Vol. GE-25, No. 1, pp. 77-82.

[17] Boerner, W-M. et al. (1990) 'Basic Equations of Radar Polarimetry and its Solutions: The Characteristic Radar Polarization States for the Coherent and Partially Polarized Cases', SPIE Vol. 1317 Polarimetry: Radar, Infrared, Visible, Ultraviolet, and X-Ray, Huntsville, AL.

[18] Boerner, W-M. et al. (July 1990) Basic Principles in Radar Polarimetry (64 pages), in "Polarimetric Technology Handbook", J.W. Battles and L.W. Root, Editor IIT-RI/ GACIAC, CHICAGO, IL (Publishers).

[19] Boerner, W-M. & Xi, A-Q. (July 1990) "The Characteristic Radar Target Polarization State Theory for the Coherent Monostatic and Reciprocal Case Using the Generalized Polarization Transformation Ratio Formulation", ARCHIV DER ELEKTRISCHEN FBERTRAGUNG, AEF, Vol 44, No. 6, pp. 273-281 (Special Issue for the 60th Birthday of Prof. Hans Brand, UENIHFT).

[20] Boerner, W-M., Yan, W-L., Xi, A-Q. & Yamaguchi, Y. (Oct. 1991) "ON THE BASIC PRINCIPLES OF RADAR POLARIMETRY (invited review): The target characteristic polarization state theory of Kennaugh, Huynen's polarization fork concept, and its extension to the partially polarized case", IEEE Proceedings, Special Issue on Electromagnetic Theory, Vol. 79, No. 10, pp. 1538-1550.

[21] Boerner, W-M., Liu, C-L., Zhang, X., (Dec. 1991), "Comparison of Optimization Procedures for 2x2 Sinclair, 3x3 Covariance, and 4x4 Mueller (Symmetric) Matrices in Coherent Radar Polarimetry and its Applications to Target versus Background Clutter Discrimination in Microwave Sensing and Imaging", Alpbach, Austria and Ispra, Italia, Dec. 01-06, 1991, Advances in Remote Sensing (EARSeL Int'l. Journal), acc. for publication, Spring 1992 (also see: W-M. Boerner, C-L. Liu, X. Zhang and V. Naik, Polarization Dependences in Ultrawideband Impulsive Radar Target versus Clutter Discrimination, SPIE'92, OE/LASE, Los Angeles Symposium, 1992 Jan. 20-25, Ultrawideband Radar Conference, Proc. SPIE 1631, paper No. 9, (24 pages), Spring 1992).

[22] Boerner, W-M. et al. (eds.), Direct and Inverse Methods in Radar Polarimetry, Proceedings of the NATO-ARW-DIMRP'88, Bad Windsheim, FRG, 1988 Sept. 18-24, NATO-ASI Series C (Math & Phys. Sci.) Vol xyz (2 Parts: 2,200 pages); Dordrecht NL: Reidel Publ. Co., Fall 1991.

[23] Born, M. & Wolf, E. (1970) Principles of Optics, 4th ed., Pergamon Press, New York.

[24] Brusmark, B. et al. (Feb. 1985) 'Digital Signal Processing for Spaceborne Synthetic Aperture Radar, National Defense Research Institute, FOA Report C 30381-E1, LinkSpping, Sweden.

[25] Bush, T.F. & Ulaby, F.T. (May 1976) 'Radar Return from a Continuous Vegetation Canopy', IEEE Trans. Ant. & Prop., Vol AP-24, No 3, pp. 269-276.

[26] Chan, C-Y. (1981) Studies on the Power Scattering Matrix of Radar Targets, M.Sc. Thesis, UIC-EECS-CL, University of Illinois at Chicago.

[27] Crosignani, B. et al. (1975) Statistical Properties of Scattered Light, Academic Press, N.Y.

[28] Dainty, J.C. (1975) Laser Speckle and Related Phenomena, in Topics in Applied Physics, Vol 9, Springer Verlag, N.Y.

[29] Dainty, J.C. (1980) 'An Introduction to "Gaussian" Speckle', Proceedings of the Soc. of Photo-Optical Instr. Engr., Vol. 243, SPIE: Applications of Speckle Phenomena.

[30] Davenport, W.B. & Root, W.L. (1958) An Introduction to the Theory of Random Signals and Noise, McGraw-Hill Book, N.Y.

[31] De Graaf, S.R. (1989) 'Statistical classification of polarimetric SAR images', URSI Radio Science Meeting, San Jose, 26-30 June 1989, p. 251.

[32] Durand, J.M. et al. (Sept 1987) 'SAR Data Filtering for-Classification', IEEE Trans. Geo. & Rem. Sens., Vol GE-25, No 5, pp. 629-637.

[33] Eaves, J.L. & Reedy, E.K. (1987) Principles of Modern Radar, Van Nostrand Reinhold, N.Y.

[34] Elachi, C. et al. (Jan. 1977) 'Models of Radar Imaging of the Ocean Surface Waves', IEEE, Vol. AP-25, No. 1, pp. 84-95.

[35] Elachi, C. et al. (Oct 1982) 'Spaceborne Synthetic-Aperture Imaging Radars: Applications, Techniques, and Technology', Proc. IEEE, Vol. 70, No. 10, pp. 1174-1209.

[36] Elachi, C. (Dec. 1982) 'Radar Images of the Earth from Space', Scientific American, Vol. 247, No. 6, pp. 54-61.

[37] Engheta, N. et al. (April 1982) 'Radar Scattering from a Diffuse Vegetation Layer Over a Smooth Surface', IEEE, Vol. GE-20, No. 2, pp. 212-216.

[38] Eom, H.J. & Boerner, W-M. (Mar 1986) "A Re-examination of Radar Terrain Backscattering at Nadir", IEEE Trans. on Geosci. & Remote Sensing, Vol. 24(2), pp. 232-234.

[39] Farina, A. et al. (Feb. 1986) 'Coherent Radar Detection in Log-Normal Clutter', IEE Proceedings, Vol 133, Pr F, No 1, pp. 39-54.

[40] Foo, B-Y., Chaudhuri, S.K., & Boerner, W.-M. (July 1990) "Polarization Correction and Extension of the Kennaugh-Cosgriff Target-Ramp Response Equation to the Bistatic Case and Applications to Electromagnetic Inverse Scattering", IEEE Trans. A&P, Vol. AP-38, No. 7, pp. 964-972.

[41] Fujii, H. & Asakura, T. (May 1974) 'Effect of Surface Roughness on the Statistical Distribution of Image Speckle Intensity', Optics Communications, Vol 11, No 1, pp. 35-38.

[42] Fung A.K. & Eom, H.J. (July 1983) 'Effects of a Rough Boundary Surface on Polarization of the Scattered Field from an Inhomogeneous Medium', IEEE T-GE, Vol GE-21, No 3, pp. 265-270.

[43] Fung A.K. & Eom, H.J (Dec. 1983) 'Scattering from a Random Layer with Applications to Snow, Vegetation and Sea Ice', IEE Proc., Vol 130, Part F, No 7, pp. 591-599.

[44] Gjessing, D.T. (1980) 'Remote Surveillance by EM Waves for Air-Water-Land, Ann Arbor Science Publishers, Ann Arbor, MI.

[45] Goodman, J.W. (1975) 'Statistical Properties of Laser Speckle Patterns', Section 2, Topics in Applied Physics Vol 9, Springer-Verlag, New York.

[46] Goodman, J.W. (1985) Statistical Optics, Wiley & Sons, NY, Chapter 2.

[47] Green, W.B. (1983) Digital Image Processing - A Systems Approach; Van Nostrand Reinhold Publ., N.Y.

[48] Hall, E.L. (1979) Computer Image Processing and Recognition Academic Press, N.Y.

[49] Hord, R.M. (1979) 'Digital Image Shape Detection', Proceedings of the National Computer Conf., 48, 7, p. 243.

[50] Hord, R.M. (1982) 'Digital Image Processing of Remotely Sensed Data', Notes and Reports in Computer Science and Applied Mathematics, Academic Press, N.Y.

[51] Hummel, R. (1977) Image Enhancement by Histogram Transformation Computer Graphics and Image Processing, 6, pp. 184-195.

[52] Huynen, J.R. (1970) Phenomenologic Theory of Radar Targets, Ph.D. Dissertation, Technical University Delft, Delft Holland.

[53] Jain, A.K. (1977) Determination of Ocean Wave Heights from Synthetic Aperture Radar Imagery, Appl. Phys, Vol 13, 371-382.

[54] Jain, A.K. & Christensen, C.R. (July 1980) 'Digital Processing of Images in Speckle Noise', Proc. SPIE, Applications of Speckle Phenomena 243, pp. 46-50.

[55] Jakeman, E. and Tough, R.J.A.: (Sept. 1987) "Generalized K distribution: a statistical model for weak scattering", JOSA A, Vol.4, No.9, Sept. 1987.

[56] Jakeman E. and Pusey, P.N.: (1978) "Significance of K distributions in Scattering Experiments", Phys. Rev. Lett. 40, pp. 546-550.

[57] Jensen, H. et al. (Oct. 1977) 'Side-Looking Airborne Radar", Scientific American, pp. 84-95.

[58] Kennaugh, E.M. (1952) Polarization Properties of Radar Reflectors, M.Sc. Thesis, Dept. Electr. Eng., Ohio State University, Columbus, Ohio.

[59] Kennaugh, E.M. (March 1981) Polarization Dependance of RCS - A Geometrical Interpretation, IEEE Trans. Ant. & Prop., Vol AP-29, No. 3, pp. 412-413.

[60] Kenney, J.F & Keeping, E.S. (1964) Mathematics of Statistics - Part I, van Nostrand (3rd ed.), N.Y.

[61] Kong, J.-A. et al. (1988) 'Identification of terrain cover using the optimum polarimetric classifier', Journal of Electromagnetic Wave and Applications, 2, pp. 171-194.

[62] Kong, J.-A. (ed.) (1990) Polarimetric Remote Sensing, PIER 3, Amsterdam, NL: Elsevier.

[63] Kostinski, A.B. & Boerner, W-M. (Dec. 1986) 'On Foundations of Radar Polarimetry', IEEE, Vol. AP-34, No. 12, pp. 1395-1404. Also see: Comments by H. Mieras, pp. 1470-1471 and the author's reply, pp. 1471-1473.

[64] Kostinski, A.B. & Boerner, W-M. (Aug. 1987) 'On the Polarimetric Contrast Optimization, IEEE, Vol. AP-35, No. 8, pp. 988-991.

[65] Kostinski, A.B., James, B.D. & Boerner, W.-M. (Jan. 1988) "On the Optimal Reception of Partially Polarized Waves", Journal of the Optical Society of America, Part A, Optics & Image Sciences, Series 2, Vol. 5, No. 1, pp. 58-64.

[66] Kostinski, A.B., James, B.D., Boerner, W-M. (Oct. 1988) 'Polarimetric Matched Filter for Radar Imaging', Can. J. Phys., Vol. 66, Issue 10, pp. 871-877.

[67] Kostinski, A.B., James, B.D. & Boerner, W.-M. (Oct. 1988) "Polarimetric Matched Filter for Coherent Imaging", Canadian Journal of Physics, Special Issue on Optics and Modern Image Processing, Vol 66, pp. 871-877.

[68] Krogager, E. (1991) 'Decomposition of the Radar Target Scattering Matrix with Application to High Resolution Target Imaging', Danish Defence Research Establishment, P.O. Box 2715, DK 2100 Copenhagen, Denmark.

[69] Leberl, F. et al. (Feb. 28, 1983) 'Sea Ice Motion Measurement from SEASAT SAR Images', J. Geophys. Res., Vol 88, No C3, pp. 1915-1928.

[70] Lewis, B.L. & Olin, I/D. (1980) 'Experimental Study and Theoretical Model of High Resolution Radar Backscatter from the Sea', Radio Science, 15, pp. 815-828.

[71] Lim, H.H. et al. (1989) 'Classification of earth terrain using polarimetric synthetic aperture radar images', Jour. of Geophys. Res., 93, pp. 7049-7057.

[72] Lim, J.S. & Nawab, H. (July 1980) 'Techniques for Speckle Noise Removal', Proc. SPIE 243, pp. 35-44.

[73] Long, M.W. (1983) Radar Reflectivity of Land and Sea, Artech, Dedham, MA.

[74] LGneburg, E. et al. (May 1991) 'Polarimetric Covariance Matrix Analysis of Random Radar Targets', AGARD - Electromagnetic Wave Propagation Panel Symposium on Target and Clutter Scattering and their Effects on Military Radar Performance, Ottawa, Canada, 6-10 May 1991.

[75] Maffett, A.L. (1989) Topics for a Statistical Description of Radar Cross Section, John Wiley & Sons, New York.

[76] McKechnie T.S. (1975) Speckle Reduction, Section 4, Topics in Applied Physics Vol 9, Springer-Verlag, New York.

[77] Mensa, D.L. (1981) High Resolution Radar Imaging, Artech House, Dedham, MA (see also updated edition).

[78] Middleton, D. (1960) Introduction to Statistical Communication Theory, McGraw-Hill, N.Y.

[79] Moore, R.K. (Nov 1978) 'Active Microwave Sensing of the Earth's Surface-A Mini Review', IEEE T-AP, Vol AP-26, No 6, pp. 843-849.

[80] Novak, L.M. & Burl, M.C. (1989) 'Optimal Speckle Reduction in POL-SAR Imagery and its Effects on Target Detection, SPIE-Proceedings Vol 1101, Orlando FL.

[81] Ohtsubo, J. & Ouchi, K. et al. (Sept. 1987) 'Statistical Properties of Speckle Intensity Variations Dependence of Speckle Statistics on Backscatter Cross-Section Fluctuations in Synthetic Aperture Radar Images of Rough Surfaces, IEEE Trans. Geo. & Rem. Sens., Vol GE-25, No 5, pp. 623-628.

[82] Olin, I.D. (Oct. 1982) 'Amplitude and Temporal Statistics of Sea Spike Clutter', IEE Int. Conf. Radar'82, pp. 198-202.

[83] Papoulis, A. (1965) Probability, Random Variables, and Stochastic Processes, McGraw-Hill, New York.

[84] Parry, G. (1975) Speckle Patterns in Partially Coherent Light, Section 3, Topics in Applied Physics Vol 9, Springer-Verlag, New York.

[85] Peake, W.H. (1968) Theory of Radar Return from Terrain, Antenna Lab: The Ohio State University, Columbus, OH.

[86] Pottier, E. (1990) Contribution of Polarimetry in the Discrimination of Radar Targets: Application to the High Resolution

Electromagnetic Radar Imaging, Ph.D. Thesis, L-Universit) de Rennes I, U.F.R. Structure et Propri)t)s de la Mati/re, France.

[87] Pratt, W.K. (1978) Digital Image Processing, N.Y., Wiley Publ.

[88] Rice, S.O. (Feb/Mar. 1951) Reflection of EM Waves from Slightly Rough Surfaces, Commun. Pure Applied Math., Vol 4, pp. 361-378.

[89] Rosenbaum S. & Bowles, L.W. (Mar. 1974) 'Clutter Return from Vegetated Areas', IEEE Trans. Ant. & Prop., Vol AP-22, No 2, pp. 227-236.

[90] Rosenfeld, A. & Kak, A.C. (1976) Digital Picture Processing, Academic Press, N.Y.

[91] Sabins, F.F. (1978) Remote Sensing, Principles and Interpretation, W.H. Freeman and Co., San Francisco.

[92] Schalkoff, R.J. (1989) Digital Image Processing and Computer Vision, John Wiley & Sons, New York, pp. 136-145.

[93] Schtzel K., (1983) "K-distributed phase differences in turbulent random phase screens", JOSA 73, pp. 269-276.

[94] Schleher, D.C. (Nov. 1976) 'Radar Detection in Weibull Clutter', IEEE-AES, Vol. AES-12, No. 6, pp. 736-743.

[95] Schowengerdt, R.A. (1983) Techniques for Image Processing and Classification in Remote Sensing; Academic Press, N.Y.

[96] Sekine, M. & Mao, Y. (1990) Weibull Radar Clutter, IEE Radar, Sonar, Navigation and Avionics Series 3, Peter Peregrinus Ltd. Publ. London.

[97] Shanmugan, S. et al. (July 1981) 'Textural Features for Radar Image Analysis', IEEE, Vol. GE-19, No. 3, pp. 153-156.

[98] Sinclair, G. (Feb. 1950) 'The Transmission and Reception of Elliptically Polarized Waves', Proc. IRE, Vol 38, pp. 148-151.

[99] Skolnik, M.I. (1981) Introduction to Radar Systems, (2nd ed.), McGraw-Hill Book, Singapore.

[100] Stratton, J.A. (1941) Electromagnetic Theory, McGraw-Hill, N.Y.

[101] Tomiyasu, K. (May 1978) 'Tutorial Review of Synthetic-Aperture Radar (SAR) with Applications to Imaging of the Ocean Surface', Proc. IEEE, Vol. 66, No. 5, pp. 563-583.

[102] Trunk, G.V. et al. (Sept. 1970) 'Detection of Targets in Non-Gaussian Sea Clutter', IEEE Trans. on Aerosp. & Eletr. Sys., AES-6, pp. 620-38.

[103] Trunk, G.V. (Mar. 1972) 'Radar Properties of Non-Rayleigh Sea Clutter', IEEE Trans. on Aerosp. & Eletr. Sys., AES-8, pp. 196-204.

[104] Twersky, V. (1951) 'On Scattering and Reflection of EM Waves by Rough Surfaces', IRE Trans., Vol AP-5, pp. 81-90.

[105] Ulaby, F.T. (July 1980) 'Vegetation Clutter Model', IEEE Trans. Ant&Prop., Vol AP-28, No 4, pp. 538-545.

[106] Ulaby, F.T et al. (1981) Microwave Remote Sensing (Active and Passive), Vol I, Addison-Wesley, Reading, MA.

[107] Ulaby, F.T et al. (1982) Microwave Remote Sensing (Active and Passive), Vol II, Addison-Wesley, Reading, MA.

[108] Ulaby, F.T. (Dec. 1982) 'Radar Signatures of Terrain: Useful Monitors of Renewable Resources', Proc. IEEE, Vol. 70, No. 12, pp. 1410-1428.

[109] Ulaby, F.T. et al. (May 1988) 'Fluctuation Statistics of Millimeter-Wave Scattering from Distributed Targets', IEEE Trans. Geo. & Remote Sens., Vol 26, No 3, pp. 268-281.

[110] Ulaby, F.T. & Elachi, C. (eds.) (1990) Radar Polarimetry for Geoscience Applications, Artech House, Inc, Norwood MA.

[111] Valenzuela G.R. (Nov. 1968) 'Scattering of EM Waves from a Tilted Slightly Rough Surface', Radio Science, Vol 3 (new series), pp. 1057-1066.

[112] Van Trees, H.L. (1968) Detection, Estimation, and Modulation Theory Part I, John Wiley & Sons, New York.

[113] Van Zyl, J.J., (1992) 'Unsupervised Classification of Scattering Behavior Using Imaging Radar Polarimetry Data', Proceedings of the NATO-ARW-DIMRP'88, Bad Windsheim, FRG, 1988 Sept. 18-24, NATO-ASI Series C (Math & Phys. Sci.) Vol xyz, Dordrecht NL: Reidel Publ. Co., Feb. 1992.

[114] Van Zyl, J.J., Papas, C.H & Elachi, C. (July 1987), 'On the Optimum Polarizations of Incoherently Reflected Waves', IEEE Trans. Antenna & Propagation, AP-35, pp. 818-825.

[115] Van Zyl, J.J., Zepker, H.A. & Elachi, C. (July/August 1987), Imaging Radar Polarization Signatures: Theory and Observations', Radio Science, 22, pp 529-543.

[116] Van Zyl, J.J. and Burnette, C.F. (April 1990), "Bayesian Classification of Polarimetric SAR Images Using Adaptive A-Priori Probabilities', International Journal of Remote Sensing, (submitted).

[117] Walther, M., (May 1992), Statistical Analysis and Enhancement of Polarimetric SAR images, M.Sc Thesis, Dept. Electr. Eng. & Comp. Sci., University of Illinois at Chicago, Chicago, Illinois.

[118] Walther, M., A.C. Segal, W-M. Boerner, (1992) "Speckle Reduction in the Development of the Polarimetric Matched Image Filter (PMIF) for the Optimization of Image Discriminants in POL-SAR Image Analysis, in W-M. Boerner et al. (eds), Direct and Inverse Methods in Radar Polarimetry, Proceedings NATO-ARW-DIMRP'88, Bad Winsheim, FRG, 1988 Sept. 18-24, NARO-ASI Series C (Math & Phys. Sci.), Vol. C-350, Pt. 2, pp. 1497-1453, Kluwer Acad. Publ./D. Reidel, Dordrecht, NL, Feb. 1992.

[119] Watson, G.S. (1983) Vol 6: Statistics on Spheres, Wiley-Interscience Publication, John Wiley & Son, N.Y.

[120] Wegman, E.J.& DePriest, D.J. (eds.) (1986) Statistical Image Processing and Graphics, Marcel Dekker, Inc. New York.

[121] Werness S.A.S (1987) 'Application of Predictive Compression Methods to Synthetic Aperture Radar Imagery I and II', Optical Engineering, Vol 26, No 12.

[122] Woodward, P.M. (1980) Probability and Information Theory, with Applications to Radar, Artech House, Dedham MA.

[123] Xi, A-Q., Boerner, W-M. (1992) "Determination of the Characteristic Polarization States of the Target Scattering Matrix [S(AB)] for the Coherent, Monostatic and Reciprocal Propagation Space", JOSA, Part 1A, Optics & Image Science, Series 2, Vol. 10, No. 3, pp. 437-455.

[124] Yamaguchi, Y., Sasugawa, K., Sengoku, M., Abe, T, Boerner, W.-M. (Dec. 14, 1989) "On the Optimal Reception of Partially Polarized Waves", Journal of the Japanese Institute of Electrical, Electronic & Communications Engineers, Transactions on Antennas & Propagation, Vol. 69, pp. 37-43 (in Japanese: English translation available).

[125] Yan, W-L. Boerner, W-M. (Oct. 1991) "Optimal Polarization States Determination of the Stokes Reflection Matrices [M] for the coherent case, and of the Mueller matrix [M] for the partially polarized case", Journal of Electromagnetic Waves and Applications, Vol 5, No. 10, pp. 1123-1150, Oct. 1991.

[126] Yaroslavsky, L.P. (1985) Digital Picture Processing - An Introduction, Springer Verlag, N.Y.

[127] Yueh, H.A. et al. (1988) 'Optimal classification of terrain cover using normalized polarimetric data', J. Geophys. Res. Vol 93, pp. 15261-15267.

[128] Zebker H.A. & Goldstein R.M. (April 10, 1986) 'Topographic Mapping from Interferometric Synthetic Aperture Radar Observations', J. Geophys. Res. Vol 91, No B5, pp. 4993-4999.

[129] Zebker, H, J.J. van Zyl, D.N. Held (Jan. 10, 1987) 'Imaging Radar Polarimetry From Wave Synthesis', Journal of Geophysical Research, Vol 92, No B1, pp. 683-701.